Heterogeneous nucleation and grain growth of inoculated aluminium alloys: An integrated study by in-situ X-radiography and numerical modelling

Yijiang Xu[1], Daniele Casari[2], Qiang Du[3], Ragnvald H. Mathiesen[2], Lars Arnberg[1], Yanjun Li[1*]

[1] Department of Materials Science and Engineering, Norwegian University of Science and Technology (NTNU), N-7491 Trondheim, Norway

[2] Department of Physics, Norwegian University of Science and Technology (NTNU), N-7491 Trondheim, Norway

[3] SINTEF Materials and Chemistry, N-7465 Trondheim, Norway

*Corresponding author: E-mail address: yanjun.li@ntnu.no

Abstract

A comprehensive study on the heterogeneous nucleation and grain growth of Al-10wt.%Cu alloys inoculated with Al-5Ti-1B was carried out. To further reveal the solute segregation stifling mechanism, in-situ near-isothermal melt solidification experiments with constant cooling rates and greatly suppressed melt convection were realized by in-situ microfocus X-radiography study. The kinetics of heterogeneous nucleation and grain growth under the isolated influence of cooling rate and addition level of inoculant particles has been quantitatively studied. Moreover, novel image processing and analysis approaches have been proposed, to determine the maximum nucleation undercooling and solid volume fraction at nucleation ceasing. To better understand the heterogeneous nucleation and grain growth behaviors under the in-situ experiment conditions, a new grain size prediction model in which both pure globular growth kinetics and dendritic growth kinetics including spherical/globular to dendritic transition (GDT) has been developed. The quantitative agreements between the simulation results and experimental results in terms of grain size, maximum nucleation undercooling and solid fraction at nucleation ceasing, have confirmed the validity of the solute segregation stifling mechanism for castings without recalescence. Furthermore, it is demonstrated that globular growth kinetics is an acceptable approximation for grain size prediction purposes of well grain-refined aluminum alloys. However, for poorly inoculated aluminum alloys with well-developed coarse dendritic grains, an application of dendritic growth kinetics significantly improves the grain size prediction power of the model.

Key words: Heterogeneous nucleation, Grain growth, Grain refinement, Solidification, Solute segregation

1. Introduction

During casting of aluminium alloys, a fine equiaxed grain structure is usually preferred, as it helps to reduce casting defects, facilitates subsequent processing and improves mechanical properties. Such a grain structure is usually obtained by inoculation using Al-Ti-B or Al-Ti-C master alloys [1-3]. An in-depth understanding on the grain refinement mechanism in terms of the nucleation potency of inoculant particles, the influence of solute and the solidification conditions has been achieved through a series of dedicated experimental and theoretical modelling studies [1-29].

In the past decades, substantial research efforts have been devoted to developing analytical and numerical models to simulate the heterogeneous nucleation behavior during solidification with the aim to predict the as-cast grain size in inoculated aluminium alloys [4, 5, 8, 9, 14, 18, 20, 21, 24, 30-33]. Maxwell and Hellawell (M-H model) [4] proposed the first numerical model to simulate the heterogeneous nucleation behavior of inoculated aluminium alloys under spatially isothermal melt solidification condition. Based on classical heterogeneous nucleation theory and diffusion-controlled spherical growth, their model demonstrated that recalescence caused by latent heat release stifles nucleation. The model also clearly revealed the growth restriction effect of solute elements on nucleated grains, which provides time for further nucleation events to occur. A major progress in the grain size prediction model development was presented by the Free Growth Model of Greer et al. [8]. The main difference of this model, in comparison to the M-H model [4] and other earlier grain size prediction models [5, 30] is that the heterogeneous nucleation of grains was treated as a deterministic and athermal process [15], where the undercooling needed for grain initiation on potent nucleating substrates was directly related to the size of inoculant particles. Similar to the M-H model [4], grain growth is treated as spherical and recalescence act as the nucleation ceasing mechanism. The model has been used to predict the grain size of standard TP-1 test [34] samples, which are supposed to have a close-to-isothermal-melt solidification, and the predicted grain sizes were in a reasonably good agreement with the measured results [5]. For such solidification cases with recalescence, most of the grain size prediction models followed the assumption of spherical growth for the initial stage of solidification [5, 10, 19, 24, 35], and some

adopted simple dendritic growth model [36], while only one recent model developed by Martorano et al. [33] included both dendritic growth kinetics and the morphology transition of grains from spherical to dendritic. In their model [33] the growth kinetics for dendritic grains is based on parabolic tip approximation [37], which makes the transition from spherical/globular to dendritic (GDT) very difficult and GDT even did not happen in most of the solidification cases they simulated. In addition to the models following M-H [4] and Greer's [8] framework, multi-phase field method (MPFM) has also been applied to simulate grain nucleation and grain growth of Al alloys [31, 38]. It has to be noted that all the models mentioned above, have been based on isothermal melt solidification assumption, where the nucleation process stops due to recalescence. The simulation results have been validated by different TP-1 type (different molds and cooling conditions from standard TP-1 test) castings. However, for most of the directional solidification cases, like Direct Chill (DC) casting and unidirectional solidification in Bridgman furnace, recalescence may be absent [11, 14, 24]. This will make the prediction of grain size by the models described above, under directional solidification without recalescence, impossible.

To overcome such challenge, research efforts have been put into development of new nucleation stifling mechanism in the last years. Quested and Greer [14] were the first to notice the influence of solute segregation zone around the growing grain on restricting further nucleation of new grains when modeling grain nucleation in directional solidification. Within the solute segregation zone, the liquid supercooling is reduced, and accordingly the nucleation of new grains needs higher supercooling. Based on this finding, they proposed the solute impingement mechanism. For spherical grain growth, a fixed relationship between the thickness of solute diffusion layer and the radius R of growing grains, namely a thickness of R from the grain envelope, was assumed as the reduced constitutional supercooling zone, where no new grains can nucleate. For dendritic grain growth, the diffusional composition profile of solutes outside the grain envelope was assumed negligible. By such improvements, the model could give an improved prediction of the grain size [14]. Based on a quantitative analysis of the solute segregation effect on nucleation, in 2011 Shu et al. [20] proposed a concept of 'solute suppressed nucleation'(SSN) and gave an analytical solution for calculation of the thickness of SSN zone. However, the SSN thickness was much overestimated [12]. At about the same time, StJohn et al. [21] proposed a similar

concept, named as 'nucleation-free zone' (NFZ), with a thickness of $\frac{4.6D}{v}\Omega$ (D is the solute diffusion coefficient in the liquid, v is the growth velocity of grain, and Ω is the solute supersaturation ratio) from the interface, which is determined by an arbitrary cut-off of the solute concentration profile in front of the planar growth interface at the solute concentration of 1% higher than the bulk liquid. In a recent work, Du and Li [24] proposed a new nucleation ceasing mechanism, namely solute segregation stifling mechanism, based on more rigorous treatments of the solute diffusion layer and the thickness of SSN zone around growing grains. Although based on isothermal melt and constant cooling rate solidification assumption, the Du-Li model [24] has been validated with a DC-casting 5182 alloy by using average cooling rates estimated from the measured secondary dendrite arm spacings. Nevertheless, there is still a lack of direct experimental verification on the grain size prediction model and the new solute segregation stifling mechanism based on isothermal melt solidification with constant cooling rate. Besides, most of the grain size prediction models [4, 8, 24] are based on globular grain growth kinetics, the validity of which is still debatable. Furthermore, debating on the thickness of solute suppressed nucleation (SSN) zone [20, 24] or nucleation-free zone (NFZ) [21, 23] is continuing [39].

Until now, experimental studies on grain refinement behavior of aluminium alloys have been mostly limited to measurement of cooling curves during solidification of TP-1 type casting samples[6, 40], differential thermal analysis (DTA) [41], ex-situ characterization of grain size of as-cast samples, and investigations of crystallographic orientation relationships between the nucleant particle and the grain [26, 42-45]. In-situ studies on the kinetics of heterogeneous nucleation and grain growth have been few. Iqbal et al. [13, 41, 46] reported a synchrotron X-ray diffraction study on the solidification of inoculated aluminium alloys, by which a real-time monitoring of grain nucleation and growth was achieved for the first time. However, the main limitation of this approach is that only a small fraction of the nucleated grains, which fulfill the Bragg diffraction condition, can be detected. It is also difficult to track the growth rate of individual grains over time as they tend to rotate in and out of diffraction condition. Besides, the determination of maximum nucleation undercooling is not possible in their experiments. In recent years, synchrotron X-radiography has been applied as a powerful tool for real-time investigations of the solidification behavior of metal alloys like dendrite growth, dendritic fragmentation, columnar-to-equiaxed transition (CET) and

grain nucleation [16, 27, 47-55]. For instance, Reinhart et al. [16, 49] studied the effect of pulling rate on columnar-to-equiaxed transition (CET) and equiaxed grain structure during directional solidification of inoculated Al-Ni alloys by synchrotron X-radiography. Prasad et al. [27] investigated the grain nucleation and growth in Al-Si alloys inoculated with Al-3Ti-1B. However, the gravity-induced convection and grain buoyancy/sedimentation is hard to avoid in these studies as a consequence of the horizontal beam configuration of synchrotron X-ray source, which necessitates a sample configuration with vertical projecting plane [29], complicating the studies of the kinetics of grain nucleation and growth. Owing to the recent advances of microfocus X-ray sources and X-ray detector systems [56], in-situ studies on the solidification behavior of metal alloys can also be achieved with microfocus X-ray radiography set-ups [29, 57-60]. Since the X-ray beam can be aligned parallel to the gravity direction while the thin foil sample can be aligned with its broad surface perpendicular to the gravity direction, melt convection effect on the nucleation and growth of grains can be greatly suppressed. A near-isothermal melt solidification of Al-Ti-B inoculated Al-Cu alloys with a temperature gradient of G~1.5 K/mm was achieved by Murphy et al. [29]. By this method, the authors have studied the effects of grain refiner addition level, cooling rate and solute concentration on the final grain density and average grain size. However, the real-time heterogeneous nucleation kinetics and the nucleation stifling mechanism were not explored.

The solid volume fraction at nucleation ceasing is a key parameter to understand the grain refinement mechanism. However, different grain size prediction models have predicted very different volume fraction values in large range. For isothermal melt solidification with recalescence, some numerical modeling results suggested that the solid volume fraction was around 0.02%-0.08% at nucleation ceasing [10, 24], which is rather small. For recalescence-free solidification cases, due to the lack of precise nucleation ceasing mechanism, the early grain size prediction models have to be based on arbitrarily predetermined thickness of SSN, R [7] or $4.6R$ [10] (for spherical grains) around growing grains of radius R, which might give solid fraction of 12.5% and 0.6%, respectively, at nucleation ceasing. In our recent model based on the solute segregation stifling mechanism, the solid fraction values of a DC-cast 5182 alloy were predicted in the range of 0.28~0.55% varying with local cooling rate [12]. Generally, it is difficult to obtain the solid fraction data experimentally. Iqbal et al. [13, 41, 46] reported that

the grain nucleation process ceases at solid fraction of 10-30%. Murphy et al. [29] measured the solid area fraction evolution based on in-situ microfocus X-radiographic images for the whole equiaxed grain solidification process of inoculated Al-Cu alloys, which is difficult to transfer into volume fraction. Mirihanage et al. [56] proposed a method to extract 3D spatial information and solid volume fraction from in-situ 2D synchrotron radiography images during columnar dendritic growth. Unfortunately, this approach cannot be used directly for polychromatic microfocus X-radiography images, since it was based on a monochromatic X-ray source.

In this work, in-situ microfocus X-radiography is employed to study the heterogeneous nucleation and grain growth behaviors of Al-5Ti-1B inoculated Al alloys during isothermal melt solidification with constant cooling rates. Isothermal melt solidification is particularly important for understanding the grain refinement mechanism and validating grain size prediction models since most of the models are based on the spatially isothermal melt solidification assumption. However, it is difficult to realize in normal casting and even standard TP-1 test conditions [14]. A constant cooling rate solidification condition will eliminate the influence of recalescence on the heterogeneous nucleation. This is important to reveal the nucleation ceasing mechanism of directional solidification, where recalescence is rarely detectable. The influence of cooling rate and addition level of inoculant particles on the heterogeneous nucleation rate, grain number density, size of nucleation free zone, maximum nucleation undercooling and solid volume fraction at nucleation ceasing will be quantitatively studied. To better understand the experimental results, a new as-cast grain size prediction model for recalescence-free solidification is proposed, in which the dendritic growth kinetics and the morphology transition of growing grains from globular to dendritic (GDT) during equiaxed grain growth are included. By comparing the modelling results with the experimental results obtained from the in-situ X-radiography study, the different grain growth kinetics used in the model, and the new nucleation stifling mechanism have been validated.

2. Experimental

2.1 Solidification experiments

The Al-10 wt.% Cu alloy used in the current study was prepared from melting 5N (99.999%) purity aluminium and 4N (99.99%) purity copper in a clay graphite crucible using a high-temperature chamber furnace. After complete melting, different levels of commercial Al-5Ti-1B master alloy were added to the melt at 750 ˚C followed by stirring to ensure a full dissolving. After 30 minutes holding at the same temperature, the melt was cast into a copper mold of 70 mm in diameter and 150 mm in height. Four ingots inoculated with different amount of Al-5Ti-1B (0, 0.01, 0.05 and 0.1 wt.% respectively) were cast. To avoid porosity, degassing by Argon was carried out before casting. In situ X-radiography samples with dimensions of 50 x 5mm and thickness of $0.2^{+0}_{-0.01}$ mm were prepared from the ingots by cutting, grinding and polishing. The samples and the corresponding sample holders were then encapsulated into glassy carbon crucibles for the in-situ solidification experiment.

The furnace used for the in-situ X-radiography was the so-called XRMON-GF Bridgman-type gradient furnace. A detailed description of the furnace and the experimental procedure can be found elsewhere [60, 61], and here only the most important information is briefly described. In this work, the thin plate samples were melted and solidified in a horizontal position, namely, the broad surface of the sample is perpendicular to the gravity direction, which significantly reduces the melt convection during solidification. By adjusting the input power of the two heating elements in the furnace, a near-isothermal melt solidification can be achieved [29, 53]. A power down technique was used to control the cooling rate during solidification, by which the latent heat released in the thin sample could be quickly extracted by the sample holder with a large heat capacity. Due to the efficient heat transfer, constant cooling rates can be achieved. During in situ solidification experiments, the samples were remelted by heating to 670 ˚C and then cooled down at constant cooling rates ranging from 0.05 to 1.5 K/s. To reduce the oxidation of the molten sample, the experiment was performed under a nitrogen atmosphere. For in-situ imaging of the solidification process, a nominal magnification of 10 was used, giving a field-of-view (FOV) of approximately 3600×2400 μm^2 and an image pixel size of 1.79 μm. Since the actual spatial resolution is a function of scintillator resolution, source size and magnification [61], for the present setup the resolution is ~6 μm. Two frame capture rates, 2 and 3 Hz, were used to record the in-situ images during solidification.

2.2 Measurement of TiB_2 particle size distribution

To extract the TiB_2 particles in the Al-5Ti-1B master alloy, a small piece of the master alloy was dissolved in a hydrochloric acid for 24 hours, by which the Al phase and Al_3Ti particles were completely dissolved. The insoluble TiB_2 particles were collected and washed by ethanol and finally dried. The TiB_2 powders were characterized with a FEI Quanta 650 FEG scanning electron microscopy (SEM), equipped with an energy dispersive spectroscopy (EDS). Image analysis of the SEM micrographs using ImageJ [62] software was performed to measure the equivalent diameter of the broad face of TiB_2 particles and obtain the size distribution.

3. Model description

3.1 Nucleation

Heterogeneous nucleation of grains on inoculated particles is treated as a deterministic process, following Greer et al.'s free growth criterion [4], namely the undercooling ΔT_{fg} required for successful initiation of a grain on a given TiB_2 particle is related to the particle diameter d by [8]:

$$\Delta T_{fg} = \frac{4\gamma}{\Delta S_v d} = \frac{4\Gamma}{d}, \quad (1)$$

where γ is the solid-liquid interfacial energy, ΔS_v is the entropy of fusion per unit volume and Γ is the Gibbs-Thomson coefficient.

3.2 Grain growth

After nucleation, the grains keep growing with globular morphology until the radius reaches the stability extrema suggested by Mullins and Sekerka [63]. Afterwards, equiaxed grains will attempt to grow with a dendritic morphology, but the transition from globular to dendritic morphology can occur only when calculated grain envelope fraction f_g is larger than the solid fraction f_s, or the internal solid fraction $f_i (= f_s/f_g)$<1; otherwise, the grains will remain globular [33, 64]. When the grains nucleated on the specific size class of inoculant particles at a specific undercooling, this class of new grains will be assigned a size class of grains *i*.

The growth rate of globular grains V_{gi} in each size class *i*, is given by an analytical solution as [24, 65]:

$$V_{gi} = \frac{dR}{dt} = \frac{D_l \cdot \Omega_i}{R_{gi}}, \quad (2)$$

where R_{gi} is the radius of growing grains in size class i, D_l is the diffusivity of the alloying element in liquid Al, and Ω_i is solute supersaturation ratio for grains of class i:

$$\Omega_i = \frac{C^*_{l,i} - C_l}{C^*_{l,i}(1-k)}. \quad (3)$$

Here k is the partition coefficient of solute element, C_l is the average solute concentration in the bulk melt and $C^*_{l,i}$ is the liquid concentration at the solid-liquid interface of grains in class i. For globular grains, $C^*_{l,gi}$ is :

$$C^*_{l,gi} = \frac{T - T_m}{m} + \frac{2\Gamma}{m \cdot R_{gi}}, \quad (4)$$

with T is the melt temperature, T_m is the liquidus temperature of pure Al and m is the slope of liquidus line in phase diagram.

When dendrites develop from growing globular grains, the equiaxed dendritic growth model originally proposed by Rappaz [66], Wang and Beckermann [67], and further improved by Martorano et al. [33] is applied. As illustrated in Fig. 1, three regions or phases are discriminated for each equiaxed dendritic grain cell, namely, solid phase *s*, interdendritic liquid phase *d* inside the grain envelope and extradendritic liquid phase *l* which is outside of the envelope. It is assumed that the concentration in the interdendritic liquid *d* is uniform and equal to the liquid concentration at the dendritic tip C^*_l. For dendritic grains, C^*_l is:

$$C^*_l = \frac{T - T_m}{m}. \quad (5)$$

To calculate the growth rate of dendritic grain envelope, V_e, two different growth kinetics of primary dendrite tips are used. One is based on hemispherical approximation for the dendrite tip, proposed by Kurz et al. [68-70]:

$$V_e = \frac{D_l \cdot m \cdot (k-1) \cdot C^*_l}{2\pi^2 \cdot \Gamma} (\Omega)^2. \quad (6)$$

The other one is based on the parabolic shaped dendrite tip growth kinetics, proposed by Lipton et al. [37] and simplified by Wang and Beckermann [67]:

$$V_e = \frac{D_l \cdot m \cdot (k-1) \cdot C_l^*}{\pi^2 \cdot \Gamma} (Iv^{-1}(\Omega))^2, \quad (7)$$

$$Iv^{-1}(\Omega) = 0.4567 \left(\frac{\Omega}{1-\Omega}\right)^{1.195}. \quad (8)$$

For dendritic growth, the evolution of internal solid fraction is calculated based on energy conservation and solute balance. With the recent improvement by Martorano et al. [33], the equiaxed grain growth model can deal with globular and dendritic grains at the same time, in which a globular grain is just a special case of a dendritic grain. The detailed derivation of this multi-grain and multi-phase model for equiaxed solidification can be found in the original work [33], and here only the main governing equations are listed.

Mass and volume balance:

$$f_l + \sum_{i=1}^{N} f_{gi} = 1, \quad (9)$$

where f_l is the volume fraction of the external liquid, f_{gi} the volume fraction of grain envelops in class i, and $\sum_{i=1}^{N} f_{gi}$ is the accumulated volume fraction of grain envelops of N size classes.

The evolution of the volume fraction of grain envelope f_{gi} is

$$\frac{df_{gi}}{dt} = S_{ldi} V_e + S_{lsi} V_{g,i}. \quad (10)$$

Here S_{ldi} is the liquid-interdendritic liquid interfacial area concentration (surface area of spherical grain envelope per unit volume) for dendritic grains in class i; S_{lsi} is the solid-liquid interface area concentration for globular grains. V_e and V_{gi} are the growth rates of dendritic grain envelope and globular grains of size class i, respectively.

The solute balance in the interdendritic liquid phase (labeled as d in Fig. 1) is

$$(1-k) C_l^* \frac{df_{si}}{dt} = \left(f_{gi} - f_{si}\right) \frac{dC_l^*}{dt} + (1-k) C_l^* S_{lsi} V_{g,i} + D_l \frac{S_{ldi}}{\delta_{li}} (C_l^* - C_l). \quad (11)$$

While solute balance in solid grain phase (labeled as s in Fig. 1) is

$$\frac{d(f_{si}C_{si})}{dt} = kC_l^*\left(\frac{df_{si}}{dt} - S_{lsi}V_{g,i}\right) + kC_{l,gi}^* S_{lsi}V_{g,i}. \tag{12}$$

Finally, the solute balance in external liquid phase (labeled as *l* in Fig. 1) is

$$\begin{aligned}\frac{d(f_l C_l)}{dt} = C_l^*\frac{df_l}{dt} + \sum_{i=1}^{N}\left[(C_l^* - C_{l,gi}^*)S_{lsi}V_{g,i}\right] + D_l\left(\sum_{i=1}^{N}\frac{S_{ldi}}{\delta_{li}}\right)(C_l^* - \\ C_l) + D_l\sum_{i=1}^{N_c}\left[\frac{S_{lsi}}{\delta_{li}}\left(C_{l,gi}^* - C_l\right)\right],\end{aligned} \tag{13}$$

where f_{si} is the volume fraction of solid phase in grains of class *i*, C_{si} and C_l the average composition of the solid phase of grains of class *i* and the average composition of the external liquid, respectively and δ_{li} is the average diffusion length in the external liquid for dendritic or globular grains of class *i,* as defined in Fig. 1. The detailed supplementary relations for these parameters are listed in Table A1 of Appendix, in which R_{gi} is the radius of the grain envelope in class *i*; and R_{fi} is the final grain radius for the grain class *i*.

3.3 Treatment of solute suppressed nucleation (SSN) zone

In the extradendritic liquid region outside of the grain envelope, using a quasi-steady state assumption for the solute diffusion field, the solute concentration profile can be approximated as [52]:

$$C_l(r) = C_0 + \frac{R_g}{r}(C_l^* - C_0)\,, \tag{14}$$

where C_0 is the bulk melt composition, C_l^* the solute concentration in the liquid at the solid/liquid interface, R_g the radius of grain envelope, and r the distance to the center of grain. Considering the transient growth nature of nucleated grains in the early stage of solidification, the thickness of solute diffusion layer δ_c is finite and dependent on the radius of the growing grain. It can be determined by using the solute conservation law:

$$\begin{aligned}\int_{R_g}^{R_g+\delta_c} 4\pi r^2(C_l^* - C_0)\frac{R_g}{r}dr + \int_{R_s}^{R_g} 4\pi r^2(C_l^* - C_0)dr \\ = \int_{R_0}^{R_s} 4\pi R^2(C_0 - kC_l^*)dR,\end{aligned} \tag{15}$$

where R_0 is the initial radius of the grain, R_s is the equivalent radius that calculated from the volume of the solid phase s in each grain when assuming the grains have a spherical shape, and kC_l^* is the solute concentration in the solid at the solid/liquid interface. It should be noted that δ_c is an equivalent diffusion layer thickness based on the solute concentration profile described by Eq. (14), and is always smaller than the maximum solute diffusion length.

The local undercooling in the surrounding liquid at a distance r to the center of grain, $\Delta T_e(r)$, can be determined according to Eq. (14). Fig. 2 schematically illustrates the liquidus temperature profile and different undercoolings of the melt surrounding a growing grain. It clearly shows that $\Delta T_e(r)$ is reduced and thus nucleation is suppressed within a fraction of the solute diffusion layer. The thickness of SSN zone δ_{SSN} (distance from the grain envelope) is determined by $\Delta T_e = \Delta T_{fg}$ [12]:

$$\delta_{SSN} = \left(\frac{\Delta T_{fg} - \Delta T_r}{\Delta T - \Delta T_{fg}}\right) \cdot R_g,\ 0 \le \delta_{SSN} \le \delta_c, \tag{16}$$

where ΔT, ΔT_r and ΔT_{fg} are the maximum undercooling in the melt, curvature undercooling and free growth undercooling for specific inoculation particles, respectively.

It should be noted that Eq. (16) remains meaningful only when $\Delta T_{fg} < \Delta T$ and $\Delta T_{fg} > \Delta T_r$. If $\Delta T_{fg} \ge \Delta T$, the corresponding inoculation particles cannot initiate new grains. Meanwhile, the upper bound of δ_{SSN} is the thickness of the solute diffusion layer δ_c.

It is assumed that the inoculant particles are uniformly distributed in the melt, and that all particles located within the SSN zone lose their ability to initiate new grains. The number fraction of these deactivated particles can be calculated by:

$$f_{SSN} = \sum_{i=1}^{N} \frac{4}{3}\pi (R_g + \delta_{SSN})_i^3 n_i \tag{17}$$

where *i* is the class number of grains, n_i is the number of the solid grains associated with size class *i,* and *N* is the total number of size classes for nucleated grains. Therefore, the number of newly activated inoculation particles (thus the number of newly formed grains), Δn is:

$$\Delta n = (1 - f_{SSN})N(d)_j - n_{0_j}, \quad (18)$$

with $N(d)_j$ as the total number of inoculant particles in size class j, and n_{0_j} the number of particles in this class that have nucleated grains.

As solidification proceeds, the solute diffusion layer will expand with grain growth. Once the SSN zones around neighbor grains impinge, the nucleation process stops, i.e. the so called 'solute soft impingement' or 'solute segregation stifling'. Here $f_{SSN} = 1$ is used as the criterion.

3.3 Model parameters

The physical parameters used in the numerical model are listed in Table 1. The input size distribution of inoculant TiB_2 particles in the model is based on the experimental measurement, and 200 size classes were applied. The total number of TiB_2 particles per unit volume of melt, N_0, per 0.1 wt.% Al-5Ti-1B addition, is determined based on tuning of one solidification sequence (Al-10Cu alloy with addition of 0.05 wt.% Al-5Ti-1B solidified under 0.5 K/s cooling rate) by using globular grain growth kinetics. The value obtained, N_0=2.5×10^{11} m^{-3} is used for all simulation cases. To simulate the in-situ solidification experiments, constant cooling rates were applied for all simulation cases in the present work. The equations in the model were solved numerically to get the main variables, namely ΔT, R_{gi}, Ω, δ_c, δ_{SSN}, f_{SSN}, n_i etc. at each time step (10^{-4} s), until the nucleation process is stopped by solute segregation stifling. The grain size $\overline{D}$ is calculated from the total grain density per unit volume N_V when nucleation stops, using the following equation [8, 71]:

$$\overline{D} = \frac{0.5}{{N_V}^3} \quad (19)$$

4. Experimental results

4.1 TiB_2 particle size distribution in Al-5Ti-1B master alloy

Fig. 3 shows a SEM micrograph of TiB_2 particles extracted from Al-5Ti-1B master alloy. Most of the particles have a plate shape with a hexagonal broad face while a few

have an irregular plate shape. By EDS analysis, Al_3Ti particles were not detected, indicating the particles have been completely dissolved by hydrochloric acid. The equivalent diameter of the broad face of ~2000 TiB_2 particles was measured by image analysis and the size distribution is shown in Fig. 4. The maximum diameter observed in the present master alloy is around 2 μm while a vast majority of particles have diameters in the range of 0.4-1.2 μm. The size distribution can be well fitted by a log-normal function as indicated by the solid line in Fig. 4, which is in agreement with the results reported previously [10, 72]:

$$\frac{N(d)}{N_0} = \frac{\Delta d}{\sigma d\sqrt{2\pi}} exp(-\frac{(ln(d) - ln(d_0))^2}{2\sigma^2}) \quad (20)$$

where $N(d)$ is the number of particles with diameter between d and $d + \Delta d$, N_0 is the total number of TiB_2 particles, the ratio $\frac{N(d)}{N_0}$ is the relative population, d_0 =0.77 μm is the geometric mean of distribution and σ=0.5 is the geometric standard deviation.

4.2 Isothermal melt solidification during in-situ study

During the in-situ X-radiography study, a fixed sample region of each alloy inoculated with different levels of grain refiners was used for solidification of all cooling rates by repeated melting and cooling. For each selected cooling rate, the same remelting and solidification sequence was repeated at least once in the same sample area. By comparing the different series of X-radiography images recorded for the same solidification condition, it is found that nearly the same number of grains form in the FOV, showing a good reproducibility of the experimental results. Such reproducibility also indicates the inoculant particles in the melt are quite stable for triggering heterogeneous nucleation.

4.2.1 Effect of cooling rate on grain nucleation and growth

The X-radiography image sequences recorded in-situ during solidification of Al-10Cu alloy inoculated with 0.05 wt.% Al-5Ti-1B at two constant cooling rates, 0.5 K/s and 0.05 K/s are shown in Fig. 5. Due to the difference in Cu concentration between the liquid and solid phases, the solid grains show a brighter contrast. The formation

sequence and the growth of each individual grain can be tracked from the image sequences. From some of the grains, equiaxed growth of primay dendrite arms along <100> directions can be clearly seen. Under both cooling conditions, equiaxed grain structures were obtained. However, the total number of grains appearing in the FOV is much higher for the 0.5 K/s cooling rate than that of 0.05 K/s. The newly formed grains turned up nearly at the same time in the two sides of FOV along the Y-axis, showing there is no appreciable temperature gradient in the Y-direction. However, it should be noted that grains appear slightly earlier in the right side of the FOV, indicating the presence of a small temperature gradient along the X-axis. This temperature gradient is ascribed to the experimental set-up of the Bridgman furnace used in the study, which only allows temperature control along the Y-axis (length direction of the sample) by adjusting the input power of heat elements above and below the FOV. Limited by the contact between the specimen and the sample holder, the temperature gradient along the X-axis across the FOV could not be completely eliminated. The temperature gradient along the X-axis can be estimated by measuring the time difference Δt and distance L between the first grains appearing at the left side and right side of the FOV. If we assume that the nucleation temperature for these two grains is the same, the temperature difference could be obtained as $\dot{T} \cdot \Delta t$, where $\dot{T}$ is cooling rate. Thus the temperature gradient could be calculated by $\frac{\dot{T} \cdot \Delta t}{L}$ and has been determined as ~0.2 K/mm. This is a rather small gradient in comparison to the standard TP-1grain refining test [73] and even lower than the 1.5 K/mm [29] gradient achieved in previous near-isothermal melt solidification studies by in-situ X-radiography. It should be noted that by a specially designed isothermal solidification furnace with radial geometry developed recently, the temperature gradient has been even further reduced [57-59].

The evolution of the total number of primary α-Al grains in the FOV and the average grain size as a function of solidification time since the first grain is observed have been extracted and plotted in Fig. 6. The average grain size is presented in the form of equivalent circular diameter of the equiaxed grains, which was obtained by measuring the area of the 2-D projection image of the grains. It should be noted that the diameter of the grains obtained by this approach is larger than the 3-D equivalent diameter calculated from the volume of grains when assuming the grains have a spherical shape. As can be seen from Fig. 5 and 6, the number of grains in the FOV increases quickly with the solidification time, i.e. decreasing melt temperature, until a maximum value is

reached and then remains constant, showing that nucleation stops. This is a direct experimental evidence to show that nucleation process ceases even during constant cooling rate solidification where no recalescence occurs.

Under the 0.5 K/s cooling rate condition, a maximum number of 146 grains in the FOV is achieved within 4.5s, corresponding to an average nucleation rate of 1.75×10^{10} $\mathrm{m^{-3}s^{-1}}$. In contrast, under 0.05 K/s cooling rate, a maximum number of 30 grains were obtained in the FOV at 15.5 s, corresponding to an average nucleation rate of 1.12×10^{9} $\mathrm{m^{-3}s^{-1}}$. These results indicate that both the nucleation rate and the final number of grains increase with the cooling rate. A similar trend was also observed by Iqbal et al.[13].

Nucleation-free zones (NFZ) around the nucleated and growing grains are clearly identified in the X-radiographic images in Fig. 5. Some of the NFZ regions are marked by yellow ellipsoids. Based on the measured TiB_2 particle size distribution, it can be calculated that there are around 240 particles with diameter larger than 1 μm in the FOV of the in-situ sample inoculated with 0.05 wt.% Al-5Ti-1B. This number is larger than any of the numbers of grains formed in the FOV during the in situ experiments, indicating that some of the inoculant particles have never acted as nucleation sites for Al grains.

At the early stage of nucleation, NFZ is due to the lack of highly potent inoculant particles (active at very low undercooling) in the region. In the final stage of nucleation, due to the impingement of SSN [14, 20, 24] zones around growing grains, all the space between the grains become nucleation-free zones. This is so called solute segregation stifling of nucleation [24]. It can also be seen that, the average distance between neighbour grains and the NFZ areas decrease with increasing cooling rate. This can be well explained by the unified nucleation ceasing criterion proposed by Du and Li [24]: Nucleation terminates when the changing rate of the liquidus temperature of the bulk melt $\dot{T}_l(C_l)$ reaches the changing rate of the bulk temperature $\dot{T}$, $\dot{T}_l(C_l) = \dot{T}$.

From Fig. 6, it can also be observed that, during the initial stage of solidification until nucleation stops, the average grain diameter increases continuously with the solidification time. At 0.5 K/s cooling rate, the average grain diameter grows from 34 μm to 160 μm in 4.5 s, giving an average grain growth rate of 14 μm/s, while at 0.05

K/s cooling rate, a 6.6 μm/s average grain growth rate is measured in the initial 15.5 s. Therefore, high cooling rate also promotes the initial stage grain growth. After nucleation stops, the equiaxed grains continue to grow, but the growth rate is much reduced due to the constrained growth owing to the solute enrichment in the intergranular regions. This can also be seen from Fig. 5a-6 and Fig. 5b-6, where the grains in the FOV have nearly the same size although they have nucleated at different solidification times.

Fig. 7a shows the evolution of the number of nucleated grains as a function of undercooling under different cooling rates. Here, the initial undercooling when the first grain nucleated in the FOV is assumed equal to the minimum undercooling needed for hetrogeneous nucleation on the measured maximum TiB_2 particle size ($d=2\ \mu m$). According to the free growth criterion [8] (Eq.(2)), this undercooling is determined as 0.48 K. It is interesting to see that, when the undercooling is small ($\leqslant$~1 K), the numbers of grains formed in the FOV under different cooling rates are nearly the same at the same undercooling values. It implies that the nucleation of grains is just a function of undercooling and independent of cooling rate at the beginning of solidification. This is because the volume fraction of grains is low at small undercooling, and therefore the solute rejection from the growing grains has little effect on the nucleation. This is a strong evidence to support the free growth model [8], where the initiation of new grains is only dependent of the number of available potent inoculant particles, which have sufficiently large diameters. However, at higher undercoolings, the number of grains increase much slower with undercooling in the low cooling rate cases. This means that the solute segregation zone around growing grains, in terms of reduced constitutional supercooling zones or SSN zone, has played an important role to suppress the further nucleation [14, 20]. Once the real cooling rate is less than the reduction rate of liquidus temperature of the remaining melt in the specimen (caused by the enrichment of solute in the residual liquid metal) [24], the nucleation process will stop. Fig. 7b shows the final grain density of the same sample as a function of cooling rate. As can be seen, higher cooling rate could promote grain nucleation, but it is not a linear relation between grain density and cooling rate, which is different from the experimental results of 0.1 wt.% grain refiner inoculated Al-20Cu alloy reported in Ref. [29].

4.2.2 Effect of addition level of Al-5Ti-1B on grain nucleation

Fig. 8a, 8b and 8c show three X-radiography images recorded after nucleation stops during solidification of Al-10wt.%Cu alloy with additions of 0.01, 0.05 and 0.1 wt.% Al-5Ti-1B under 0.5 K/s cooling rate, respectively. The corresponding evolution of the number of equiaxed grains formed in the FOV as a function of solidification time is shown in Fig. 6d. As can be seen, with addition of 0.01 wt.% Al-5Ti-1B, only about 12 equiaxed grains have formed in the FOV and the grains have highly branched dendrite arms. The primary dendrite arms are thin and straight, and the average length can reach ~1000 μm. For the alloys inoculated with 0.05 and 0.1 wt.% Al-5Ti-1B, 146 and 190 equiaxed grains have formed in the FOV, respectively. It should be noted that, for the alloy inoculated with 0.01 wt.% Al-5Ti-1B, columnar dendrites (not shown here) rather than fully equiaxed grains have formed in the FOV when the cooling rate is less than 0.5 K/s owing to the existence of a temperature gradient. In contrast, with 0.05 and 0.1 wt.% Al-5Ti-1B addition levels, equiaxed grain structures always formed in the range of 0.05 - 1 K/s cooling rate. It clearly shows the strong effect of inoculation on enhancing equiaxed grain solidification.

4.2.3 Maximum nucleation undercooling

Since it is impossible to measure the temperature of the specimen directly during solidification in the X-radiographic set-up, the maximum nucleation undercooling for each solidification case has to be determined indirectly. Because a temperature gradient only exists along the X-axis, while there is no temperature gradient along the Y-axis, the maximum nucleation undercooling could be calculated by:

$$\Delta T_{n,max} = \dot{T}\left(t_f - t_0\right) - \Delta T_X + \Delta T_{n,min} \quad (21)$$

where t_f and t_0 are the times when the last grain and the first grain shows up in the FOV, respectively. ΔT_X is the temperature difference between the right side and left side of the FOV due to the temperature gradient along the X-axis, and $\Delta T_{n,min}$ is the possible minimum nucleation undercooling to enable free growth of grains on the maximum sized TiB_2 particles. For a TiB_2 particle with diameter of 2 μm, $\Delta T_{n,min}$ = 0.48 K .

By this method, the $\Delta T_{n,max}$ values determined for the alloy inoculated with different amounts of Al-5Ti-1B solidified under different cooling rates are shown in Fig. 9. As

can be observed, $\Delta T_{n,max}$ is strongly dependent of the cooling rate and the addition level of grain refiner. $\Delta T_{n,max}$ increases with increasing cooling rate and decreasing inoculation level. It should be noted that the major uncertainty of the measured value stems from the time dealy for identificaiton of the appearence of the grains, which is dependent of the image capturing frequence and cooling rate. For example, at the 2 Hz image capture frequency applied in the experiment a 0.5 K uncertainty at 1 K/s can be obtained. This uncertainty has been included in Fig. 9.

4.2.4 Volume fraction of equiaxed grains at nucleation ceasing

To understand the nucleation mechanism, it is important to determine the volume fraction of solid grains when the grain nucleation process stops. Since the in-situ image only shows the 2D projection of the grains, the relation between the intensity and the thickness of the local regions of the solid grains have to be determined quantitatively. A theoretical analysis is performed, employing a formalism similar to that used for monochromatic X-radiography [56], but modified to account for the polychromatic incident X-rays used in the present experiment. The detailed approach is shown in the appendix.

The volume fraction of α-grains of inoculated alloys at maximum nucleation undercooling was measured and the results are shown in Fig. 10. As can be seen, the solid volume fraction at nucleation ceasing increases with cooling rate. This trend is in a good agreement with the experimental results reported by Iqbal et al. [13]. For the alloy inoculated with 0.05 wt.% Al-5Ti-1B, solidified at a lower cooling rate of 0.05 K/s, the volume fraction can be as low as 1.3%. In addition, the solid fraction at nucleation ceasing decreases with increasing addition level of grain refiner. To evaluate the volume fraction values extracted from the X-radiography images, the volume fraction of solid grains at maximum nucleation undercooling is also calculated by Scheil equation:

$$f_s = 1 - \left(\frac{C_0}{C_0 - \frac{\Delta T}{m}} \right)^{\left(\frac{1}{1-k}\right)}, \tag{22}$$

where C_0 is the nominal composition of solute element, and ΔT is the maximum nucleation undercooling determined in Section 4.2.3. m and k are assumed constant and

the values listed in Table 1 are employed. The results are also presented in Fig. 10. As can be seen, the experimentally determined volume fraction of solid phase is very close to that predicted by Scheil model, especially for high cooling rate (≥0.5 K/s) conditions. At lower cooling rates, the measured solid volume fraction is lower than that Scheil model predicted. The deviation from Scheil prediction is as expected since Scheil model is based on planar growth and complete liquid mixing assumptions without taking nucleation undercooling into account, while the experiment is equiaxed grain solidification with heterogeneous nucleation and with little convection in the liquid. The modelling work by Rappaz and Thevoz [66] and Wu and Ludwig [74] also showed that, Scheil model predicts larger values of solid fraction than their numerical models for equiaxed dendritic growth in the initial stage of solidification. The experimental results of solid fraction extracted from synchrotron X-ray radiography images of columnar dendritic growth reported by Mirihanage et al. [56] shows that measured solid fraction is smaller than Scheil prediction at low volume fraction (f_s <10%) but larger than Scheil prediction when f_s reaches 15%.

5. Modelling results

5.1 Modelling the grain nucleation and growth

5.1.1 Grain size prediction

Fig. 11 shows the predicted grain size of Al-10Cu alloy inoculated by 0.05 wt.% (a) and 0.1 wt.% (b) Al-5Ti-1B master alloy as a function of cooling rate in comparison to the experimentally determined grain sizes from in-situ X-radiography. As can be seen, the predicted grain sizes based on all the three growth kinetics show quantitatively good agreement with the measured values. If comparing the two addition levels of grain refiners, one can see that the predicted grain sizes at the addition level of 0.05 wt.% are closer to the measured grain sizes than at the addition level of 0.1wt.%. In the latter case, the predicted grain sizes are mostly smaller than the measured grain sizes. This can be partly attributed to that the input value for total number of inoculant particles is tuned based on the solidification condition of 0.05 wt.% addition level of master alloy and 0.5K/s cooling rate. On the other hand, this result implies that the number density of inoculant particles in the liquid metal may not increase linearly with addition level of master alloy, due to the ease of agglomeration of TiB_2 particles at higher density [75, 76].

It is interesting to see that the predicted grain sizes based on the pure globular grain growth kinetics and the parabolic dendritic tip growth kinetics are almost the same at low cooling rates. This is because GDT only happens in the solidification cases with cooling rates larger than 0.5 K/s during simulation when using the parabolic dendrite tip growth kinetics. In contrast, when the hemispherical dendrite tip growth kinetics is applied, GDT occurs in all the experimental cooling rate conditions, indicating that this growth kinetics is more sensitive to GDT. As shown in both Fig. 11a and 11b, at higher cooling rates (≥0.5 K/s), the difference in predicted grain size by using the three different growth kinetics is rather small (less than 10 μm or 3.1%). It means that GDT and subsequent dendritic growth kinetics have rather limited influence on the grain size prediction at high cooling rates. However, at low cooling rates (≤0.1 K/s), the dendritic growth kinetics has a more significant influence on the predicted grain size. As shown in Fig. 11b, at grain refiner addition level of 0.1 wt.%, the hemispherical dendrite tip growth kinetics may give a better grain size prediction for low cooling rate solidification cases with a further tuning of total number of the TiB_2 particles.

5.1.2 Maximum nucleation undercooling

Since the globular plus parabolic dendrite tip growth kinetics gives nearly the same prediction results as globular grain growth kinetics at low cooling rates and closely similar results as the hemispherical dendrite tip growth kinetics at high cooling rates, in the following parts only the hemispherical dendrite tip growth kinetics will be compared with the globular grain growth kinetics. Fig. 12 shows the predicted maximum nucleation undercooling ($\Delta T_{n,max}$) based on two growth kinetics in comparison to the in-situ experimental results. As can be seen, the predicted results are in a reasonable agreement with the experimental data. For a lower addition level of master alloy (Fig. 12a) and low cooling rates (≤0.25 K/s), the predicted $\Delta T_{n,max}$ based on pure globular growth are slightly smaller than those based on globular plus dendritic growth, while for high cooling rates (≥0.5 K/s) the prediction results are nearly the same. At 0.1 wt.% addition level of master alloy, the predicted $\Delta T_{n,max}$ values are larger than the measured ones. Since a larger $\Delta T_{n,max}$ means a smaller grain size, the simulated evolution of $\Delta T_{n,max}$ as a function of cooling rate is consistent with that of predicted grain size.

5.1.3 Solid fraction at nucleation ceasing

Fig. 13 shows the predicted and experimentally determined volume fractions of grains (f_s) at nucleation ceasing as a function of applied cooling rate at 0.05 wt.% Al-5Ti-1B addition level. With both growth kinetics, the predicted solid fraction at nucleation ceasing shows a clear dependency of the cooling rate, in agreement with the experimental results. The predicted volume fraction based on the pure globular growth kinetics are in the range of 0.9%-6.7%, which is very close to the measured values of 1.3%-7.3%, showing that this grain growth kinetics is more sensitive to the volume fraction development of solid grains. It should be noted that the predicted solid fraction of grains here is much larger than the predicted results for isothermal melt solidification with recalescence [10, 24]. When the dendritic growth kinetics is applied, the predicted solid fraction is larger than the experimental results and the difference between the predicted and measured volume fraction is even larger at higher cooling rates. This implies that the dendritic growth kinetics applied in the present work may have a tendency to overestimate the grain growth at high cooling rates.

5.1.4 Nucleation rate

The simulated nucleation rates, with a unit of $m^{-3}K^{-3}$, as a function of undercooling were extracted and compared with the experimental results. The solidification case with an addition of 0.05 wt.% Al-5Ti-1B and a cooling rate of 1 K/s is shown in Fig. 14a. It is interesting to see that the predicted nucleation rate curves show a log normal distribution shape and a quantitatively good agreement with the measured results. Both the predicted and experimentally determined nucleation rate reaches a maximum at an undercooling of ~1.0 K. In the latest stage of nucleation, i.e. in the long tale of nucleation rate curve at higher undercooling, the nucleation rate is very low. This is the reason that, although the predicted maximum nucleation undercooling is higher than that measured (Fig. 12a), the predicted grain size is very close to the measured grain size (Fig. 11a). It can also be observed from Fig. 14a that the predicted nucleation rates based on the two different grain growth kinetics are very close (the same before GDT), indicating that the grain growth kinetics used in the model has very limited influence on the predicted nucleation kinetics at high cooling rate solidification cases.

Fig. 14b shows the solidification case of 0.1 K/s cooling rate for the same alloy (inoculated with 0.05 wt.% Al-5Ti-1B). As can be seen, the predicted nucleation rate curves show a reasonable agreement with the experimental results. After GDT, the

modelling results based on dendritic growth kinetics exceed those based on globular grain growth, which means the morphology transition and subsequent dendritic growth promote heterogeneous nucleation at this low cooling rate. Besides, the peak value of the nucleation rate predicted by the model considering dendritic growth is very close to the maximum nucleation rate measured from the experiment. In comparison to the higher cooling rate case shown in Fig. 14a, the nucleation rate curves show a similar shape in the initial stage of nucleation, but a different shape (without tails) in the later stage. The maximum nucleation rate at cooling rate of 1 K/s is also larger than that of the solidification case at 0.1 K/s cooling rate, consistent with the experimental result.

5.2 Modelling the grain nucleation and growth of poorly-refined alloy

In this section, the solidification cases where the alloy is inoculated by an extremely low level of grain refiner, 0.01 wt.% Al-5Ti-1B, solidified under constant cooling rates within 0.5-1 K/s were studied. Fig. 15a shows the predicted grain size as a function of cooling rate based on three different grain growth kinetics in comparison to the in-situ experimental results. As can be seen, the prediction results based on the two dendritic growth kinetics are much larger than the globular growth kinetics, and are much closer to the experimental results. Fig. 15b compares the predicted solid fraction of grains at nucleation ceasing and the measured values obtained from the in-situ experiments. As can be seen, the model based on dendritic growth kinetics, and particularly the globular plus hemispherical dendrite tip growth kinetics, predicts much closer results to the experimental data than globular growth kinetics. It indicates that GDT and subsequent dendritic growth have a great influence on the predicted grain size for solidification of poorly grain refined alloys, for which the dendritic growth kinetics clearly has to be taken into account in grain size prediction models.

6. Discussion

Since recalescence does not happen or is insignificant in most of the directional solidification cases, it is important to develop more precise nucleation ceasing models to make grain size prediction possible for such cases. This work provides the first rigorous evaluation of the newly developed solute segregation stifling mechanism, by comparing the model prediction results with experimental results obtained from well-controlled in-situ X-radiography near-isothermal solidification studies. Based on the

quantitative agreements between the predicted and measured grain size, maximum nucleation undercooling, solid volume fraction at nucleation ceasing, and nucleation rate, it can be concluded that the proposed solute segregation nucleation stifling model is reliable.

Moreover, the good agreement between the model prediction and experimental results further confirms the importance of the precise treatments of the solute diffusion layer around growing grains. It is worth noting that the analytical solution of solute diffusion length like equivalent boundary layer 2D/V [70, 77] or characteristic diffusion length D/V [78] for steady state planar or dendritic growth cannot be used in the initial stage of solidification, which will result in overestimation of solute diffusion length [19, 20] and consequently its effect on nucleation. This is because both the solute diffusion field and equiaxed grain growth until the nucleation process stops are generally far away from the steady state. Instead, the thickness of the solute diffusion layer should be calculated based on solute conservation, as adopted in the present work. Also, both the experimental and numerical modelling results clearly show that the solid volume fraction at nucleation ceasing varies with inoculation level and cooling rate, indicating the big limitation of the assumption of fixed relationship between thickness of solute suppressed nucleation (SSN) zone and radius of growing grain when used for grain size prediction models. In contrast, the thickness of the SSN zone should be calculated in real-time during grain growth according to the solute concentration profile, the local undercooling in the solute diffusion layer as well as the size and number of inoculant particles. It is too rough to use arbitrary δ_{SSN} values.

The globular/spherical grain growth kinetics has been widely applied in grain sized prediction models of inoculated aluminium alloys [4, 5, 8, 10, 24, 25]. This is based on an argument that for the solidification of inoculated alloys, the solid fraction is rather low (0.02-0.08% [8, 10, 24]) when the nucleation process is stopped by recalescence, and therefore the influence of globular to dendritic transition (GDT) and dendritic growth kinetics on grain nucleation may be negligible. In the present work, the globular growth kinetics is further tested with isothermal melt solidification cases without recalescence, where the solid fraction of grains at nucleation ceasing (measured value of 1.3-7.3%) is much larger than the cases with recalescence. The predicted grain sizes based on the globular grain growth model are still quantitatively in good agreement with the experimental results. The prediction power of the model based on the globular

grain growth kinetics should be attributed to the correct prediction of the solid fraction of grains at nucleation ceasing (Fig. 13), which determines the thickness of SSN and the total number of inoculant particles de-activated by SSN. This is clearly reflected in the predicted nucleation rate (Fig. 14) and maximum nucleation undercooling (Fig. 12). From Fig. 11, it can be seen that the difference in the predicted grain size based on globular grain growth kinetics and dendritic growth kinetics is marginal, which is particularly obvious for high cooling rate and high grain refiner addition levels. Since the model has been validated for solidification cases with cooling rate as low as 0.05 K/s and grain refiner addition level as low as 0.05 wt.%, So, from the grain size prediction point of view, the influence of GDT and dendritic growth can be ignored for well-refined aluminium alloys.

However, the globular growth kinetics cannot well capture the grain envelope development of coarse equiaxed grains. This is clearer for solidification of alloy inoculated with extremely low addition levels of grain refiner (Fig. 8a), where the grain growth is less constrained by the adjacent surrounding grains and the grains could grow freely into coarse equiaxed dendrites with well-developed and long primary arms. With such solidification cases, the average dendrite tip velocity of grains until nucleation ceasing is much higher than for the well-refined cases, which is far beyond the globular grain growth kinetics. This is also the reason that the model based on globular grain growth kinetics tends to predict much smaller grain sizes (Fig. 15a). In these cases, the dendritic growth kinetics and GDT have to be included in the model. Furthermore, for solidification microstructure modelling of inoculated aluminium alloys, which includes heterogeneous nucleation, grain growth and even the final eutectic reaction, such a growth kinetics is more robust.

7. Conclusions

A systematic study on the heterogeneous nucleation and grain growth during isothermal melt solidification of Al-5Ti-1B inoculated Al-10wt.%Cu alloys has been conducted through a combination of the in-situ X-radiography and numerical modelling approaches.

By in-situ X-radiography experiments, the nucleation and growth kinetics of equiaxed grains under the influence of addition level of inoculation particles and cooling rate are clearly revealed during isothermal melt solidification with constant cooling rate. High

cooling rate and high inoculation level promote heterogeneous nucleation and therefore fine equiaxed grain structures. In the early stage of nucleation when the undercooling in the melt is small, the number density of nucleated grains is dominated by the available potent inoculant particles and undercooling in the melt. At higher undercoolings, the number density of nucleated grains is dominated by the thickness of the SSN zones. The experimental results also confirm that nucleation process of grains under recalescence-free solidification conditions stops due to the solute segregation stifling mechanism.

Besides, novel image processing and analysis approaches have been proposed and evaluated for quantitative determination of the volume fraction of grains at nucleation ceasing and maximum nucleation undercooling. It shows that both the maximum nucleation undercooling and solid volume fraction at nucleation ceasing increase with increasing cooling rate while decrease with addition level of inoculation particles.

A new as-cast grain size prediction model has been developed for inoculated aluminium alloys, where both the globular and dendritic grain growth kinetics are implemented and the solute segregation stifling mechanism is coupled. For the dendritic growth kinetics, both the hemispherical and the parabolic dendrite tip approximations and their influence on GDT have been evaluated. The modelling results show a good quantitative agreement with the in-situ experimental results, in terms of grain size, maximum nucleation undercooling, solid fraction at nucleation ceasing and nucleation rate, which proves the validity of the solute segregation stifling mechanism. It also confirms the importance of a proper treatment of the SSN zone for grain size prediction models.

For the alloy inoculated with normal addition levels of grain refiner, the model based on different grain growth kinetics show marginal difference in predicted grain size. It demonstrates that globular grain growth is an acceptable approximation for grain size prediction purpose for well-refined aluminum alloys, where GDT and dendritic growth have limited influence on the nucleation kinetics. However, for poorly-refined aluminium alloys with coarse and well developed equiaxed grains, and normally grain refined alloys solidifying under low cooling rate conditions, it is important to take the dendritic growth kinetics into account. It has been observed that the simulation results based on the globular plus hemispherical dendrite tip growth kinetics have a better agreement with the measured grain size, in contrast to a purely globular grain growth

kinetics. In comparison to the parabolic dendrite tip growth kinetics, the model based on hemispherical dendrite approximation is more sensitive to the GDT.

Acknowledgments

This research work has been supported by a KPN Project, PRIMAL (project number: 236675), in Norway. The financial support by The Research Council of Norway and industrial partners, Hydro Aluminium AS and Alcoa Norway AS is gratefully acknowledged.

References

[1] D.G. McCartney, Grain refining of aluminium and its alloys using inoculants, Int. Mater. Rev. 34(1) (1989) 247-260.
[2] B.S. Murty, S.A. Kori, M. Chakraborty, Grain refinement of aluminium and its alloys by heterogeneous nucleation and alloying, Int. Mater. Rev. 47(1) (2002) 3-29.
[3] T.E. Quested, Understanding mechanisms of grain refinement of aluminium alloys by inoculation, Mater. Sci. Technol. 20(11) (2004) 1357-1369.
[4] I. Maxwell, A. Hellawell, A simple model for grain refinement during solidification, Acta Metall. 23(2) (1975) 229-237.
[5] P. Desnain, Y. Fautrelle, J.L. Meyer, J.P. Riquet, F. Durand, Prediction of equiaxed grain density in multicomponent alloys, stirred electromagnetically, Acta Metall. 38(8) (1990) 1513-1523.
[6] M. Johnsson, L. Backerud, G. Sigworth, Study of the mechanism of grain refinement of aluminum after additions of Ti- and B-containing master alloys, Metall. Trans. A 24(2) (1993) 481-491.
[7] P. Schumacher, A.L. Greer, J. Worth, P.V. Evans, M.A. Kearns, P. Fisher, A.H. Green, New studies of nucleation mechanisms in aluminium alloys: implications for grain refinement practice, Mater. Sci. Technol. 14(5) (1998) 394-404.
[8] A.L. Greer, A.M. Bunn, A. Tronche, P.V. Evans, D.J. Bristow, Modelling of inoculation of metallic melts: application to grain refinement of aluminium by Al–Ti–B, Acta Mater. 48(11) (2000) 2823-2835.
[9] M.A. Easton, D.H. StJohn, A model of grain refinement incorporating alloy constitution and potency of heterogeneous nucleant particles, Acta Mater. 49(10) (2001) 1867-1878.
[10] T.E. Quested, A.L. Greer, The effect of the size distribution of inoculant particles on as-cast grain size in aluminium alloys, Acta Mater. 52(13) (2004) 3859-3868.
[11] T.E. Quested, A.L. Greer, Modelling of microstructural evolution in Bridgman specimens, Minerals, Metals & Materials Soc, Warrendale, 2004.
[12] M. Easton, D. StJohn, An analysis of the relationship between grain size, solute content, and the potency and number density of nucleant particles, Metall. Mater. Trans. A 36(7) (2005) 1911-1920.
[13] N. Iqbal, N.H. van Dijk, S.E. Offerman, M.P. Moret, L. Katgerman, G.J. Kearley, Real-time observation of grain nucleation and growth during solidification of aluminium alloys, Acta Mater. 53(10) (2005) 2875-2880.

[14] T.E. Quested, A.L. Greer, Grain refinement of Al alloys: Mechanisms determining as-cast grain size in directional solidification, Acta Mater. 53(17) (2005) 4643-4653.
[15] T.E. Quested, A.L. Greer, Athermal heterogeneous nucleation of solidification, Acta Mater. 53(9) (2005) 2683-2692.
[16] G. Reinhart, N. Mangelinck-Noël, H. Nguyen-Thi, T. Schenk, J. Gastaldi, B. Billia, P. Pino, J. Härtwig, J. Baruchel, Investigation of columnar–equiaxed transition and equiaxed growth of aluminium based alloys by X-ray radiography, Mater. Sci. Eng. A 413–414 (2005) 384-388.
[17] M.X. Zhang, P.M. Kelly, M.A. Easton, J.A. Taylor, Crystallographic study of grain refinement in aluminum alloys using the edge-to-edge matching model, Acta Mater. 53(5) (2005) 1427-1438.
[18] M. Qian, P. Cao, M.A. Easton, S.D. McDonald, D.H. StJohn, An analytical model for constitutional supercooling-driven grain formation and grain size prediction, Acta Mater. 58(9) (2010) 3262-3270.
[19] H. Men, Z. Fan, Effects of solute content on grain refinement in an isothermal melt, Acta Mater. 59(7) (2011) 2704-2712.
[20] D. Shu, B. Sun, J. Mi, P.S. Grant, A quantitative study of solute diffusion field effects on heterogeneous nucleation and the grain size of alloys, Acta Mater. 59(5) (2011) 2135-2144.
[21] D.H. StJohn, M. Qian, M.A. Easton, P. Cao, The Interdependence Theory: The relationship between grain formation and nucleant selection, Acta Mater. 59(12) (2011) 4907-4921.
[22] Z. Fan, An epitaxial model for heterogeneous nucleation on potent substrates, Metall. Mater. Trans. A 44(3) (2013) 1409-1418.
[23] A. Prasad, L. Yuan, P.D. Lee, D.H. StJohn, The Interdependence model of grain nucleation: A numerical analysis of the Nucleation-Free Zone, Acta Mater. 61(16) (2013) 5914-5927.
[24] Q. Du, Y.J. Li, An extension of the Kampmann-Wagner numerical model towards as-cast grain size prediction of multicomponent aluminum alloys, Acta Mater. 71 (2014) 380-389.
[25] Q. Du, Y.J. Li, Prediction of As-Cast Grain Size of Inoculated Multicomponent Aluminum Alloys, Mater. Sci. Forum 790-791 (2014) 185-190.
[26] Z. Fan, Y. Wang, Y. Zhang, T. Qin, X.R. Zhou, G.E. Thompson, T. Pennycook, T. Hashimoto, Grain refining mechanism in the Al/Al–Ti–B system, Acta Mater. 84(0) (2015) 292-304.
[27] A. Prasad, S.D. McDonald, H. Yasuda, K. Nogita, D.H. StJohn, A real-time synchrotron X-ray study of primary phase nucleation and formation in hypoeutectic Al–Si alloys, J. Cryst. Growth 430 (2015) 122-137.
[28] M.A. Easton, M. Qian, A. Prasad, D.H. StJohn, Recent advances in grain refinement of light metals and alloys, Curr. Opin. Solid State Mat. Sci. 20(1) (2016) 13-24.
[29] A.G. Murphy, W.U. Mirihanage, D.J. Browne, R.H. Mathiesen, Equiaxed dendritic solidification and grain refiner potency characterised through in situ X-radiography, Acta Mater. 95(0) (2015) 83-89.
[30] P. Thévoz, J.L. Desbiolles, M. Rappaz, Modeling of equiaxed microstructure formation in casting, Metall. Trans. A 20(2) (1989) 311-322.
[31] S. Nomoto, S. Minamoto, K. Nakajima, Numerical simulation for grain refinement of aluminum alloy by multi-phase-field model coupled with CALPHAD, ISIJ inter. 49(7) (2009) 1019-1023.

[32] M. Bedel, K.O. Tveito, M. Založnik, H. Combeau, M. M'Hamdi, A model study of the impact of the transport of inoculant particles on microstructure formation during solidification, Comput. Mater. Sci. 102(0) (2015) 95-109.
[33] M. Martorano, D. Aguiar, J. Arango, Multigrain and Multiphase Mathematical Model for Equiaxed Solidification, Metall. Mater. Trans. A 46(1) (2015) 377-395.
[34] Standard Test Procedure for Aluminium Alloy Grain Refiners: TP-1, The Aluminum Association, Washington,DC, 1987.
[35] R. Günther, C. Hartig, R. Bormann, Grain refinement of AZ31 by (SiC)P: Theoretical calculation and experiment, Acta Mater. 54(20) (2006) 5591-5597.
[36] W.U. Mirihanage, D.J. Browne, Combined analytical/numerical modelling of nucleation and growth during equiaxed solidification under the influence of thermal convection, Comput. Mater. Sci. 46(4) (2009) 777-784.
[37] J. Lipton, M.E. Glicksman, W. Kurz, Dendritic growth into undercooled alloy metals, Mater. Sci. Eng. 65(1) (1984) 57-63.
[38] B. Böttger, J. Eiken, M. Apel, Phase-field simulation of microstructure formation in technical castings – A self-consistent homoenthalpic approach to the micro–macro problem, J. Comput. Phys. 228(18) (2009) 6784-6795.
[39] D.H. StJohn, A. Prasad, M.A. Easton, M. Qian, The Contribution of Constitutional Supercooling to Nucleation and Grain Formation, Metall. Mater. Trans. A (2015) 1-18.
[40] M. Johnsson, Grain refinement of aluminium studied by use of a thermal analytical technique, Thermoch. Acta 256(1) (1995) 107-121.
[41] N. Iqbal, N.H. van Dijk, S.E. Offerman, N. Geerlofs, M.P. Moret, L. Katgerman, G.J. Kearley, In situ investigation of the crystallization kinetics and the mechanism of grain refinement in aluminum alloys, Mater. Sci. Eng. A 416(1–2) (2006) 18-32.
[42] K.F. Kobayashi, S. Hashimoto, P.H. Shingu, Nucleation of aluminum by Al3Ti in the Al-Ti system, Z. Metallkund. 74(11) (1983) 751-754.
[43] A. Tronche, A.L. Greer, Electron back-scatter diffraction study of inoculation of Al, Philos. Mag. Lett. 81(5) (2001) 321-328.
[44] Z. Chen, H. Kang, G. Fan, J. Li, Y. Lu, J. Jie, Y. Zhang, T. Li, X. Jian, T. Wang, Grain refinement of hypoeutectic Al-Si alloys with B, Acta Mater. 120 (2016) 168-178.
[45] F. Wang, D. Qiu, Z.-L. Liu, J.A. Taylor, M.A. Easton, M.-X. Zhang, The grain refinement mechanism of cast aluminium by zirconium, Acta Mater. 61(15) (2013) 5636-5645.
[46] N. Iqbal, N.H. van Dijk, S.E. Offerman, M.P. Moret, L. Katgerman, G.J. Kearley, Nucleation kinetics during the solidification of aluminum alloys, J. Non-Cryst. Solids 353(32–40) (2007) 3640-3643.
[47] P.D. Lee, J.D. Hunt, Hydrogen porosity in directional solidified aluminium-copper alloys:in situ observation, Acta Mater. 45(10) (1997) 4155-4169.
[48] R.H. Mathiesen, L. Arnberg, X-ray radiography observations of columnar dendritic growth and constitutional undercooling in an Al–30wt%Cu alloy, Acta Mater. 53(4) (2005) 947-956.
[49] H. Nguyen-Thi, G. Reinhart, N. Mangelinck-Noël, H. Jung, B. Billia, T. Schenk, J. Gastaldi, J. Härtwig, J. Baruchel, In-Situ and Real-Time Investigation of Columnar-to-Equiaxed Transition in Metallic Alloy, Metall. Mater. Trans. A 38(7) (2007) 1458-1464.
[50] D. Ruvalcaba, R.H. Mathiesen, D.G. Eskin, L. Arnberg, L. Katgerman, In situ observations of dendritic fragmentation due to local solute-enrichment during directional solidification of an aluminum alloy, Acta Mater. 55(13) (2007) 4287-4292.

[51] S. Boden, S. Eckert, G. Gerbeth, Visualization of freckle formation induced by forced melt convection in solidifying GaIn alloys, Mater. Lett. 64(12) (2010) 1340-1343.
[52] Q. Dong, J. Zhang, J. Dong, H. Xie, Z. Li, Y. Dai, Y. Liu, B. Sun, In situ observation of columnar-to-equiaxed transition in directional solidification using synchrotron X-radiation imaging technique, Mater. Sci. Eng. A 530 (2011) 271-276.
[53] A. Bogno, H. Nguyen-Thi, G. Reinhart, B. Billia, J. Baruchel, Growth and interaction of dendritic equiaxed grains: In situ characterization by synchrotron X-ray radiography, Acta Mater. 61(4) (2013) 1303-1315.
[54] K. Nogita, H. Yasuda, A. Prasad, S.D. McDonald, T. Nagira, N. Nakatsuka, K. Uesugi, D.H. StJohn, Real time synchrotron X-ray observations of solidification in hypoeutectic Al–Si alloys, Mater. Character. 85(0) (2013) 134-140.
[55] E. Liotti, A. Lui, R. Vincent, S. Kumar, Z. Guo, T. Connolley, I.P. Dolbnya, M. Hart, L. Arnberg, R.H. Mathiesen, P.S. Grant, A synchrotron X-ray radiography study of dendrite fragmentation induced by a pulsed electromagnetic field in an Al–15Cu alloy, Acta Mater. 70 (2014) 228-239.
[56] W.U. Mirihanage, K.V. Falch, I. Snigireva, A. Snigirev, Y.J. Li, L. Arnberg, R.H. Mathiesen, Retrieval of three-dimensional spatial information from fast in situ two-dimensional synchrotron radiography of solidification microstructure evolution, Acta Mater. 81(0) (2014) 241-247.
[57] M. Becker, C. Dreißigacker, S. Klein, F. Kargl, Near-isothermal furnace for in situ and real time X-ray radiography solidification experiments, Rev. Sci. Instrum. 86(6) (2015) 063904.
[58] A.G. Murphy, R.H. Mathiesen, Y. Houltz, J. Li, C. Lockowandt, K. Henriksson, N. Melville, D.J. Browne, Direct observation of spatially isothermal equiaxed solidification of an Al–Cu alloy in microgravity on board the MASER 13 sounding rocket, J. Cryst. Growth 454 (2016) 96-104.
[59] A.G. Murphy, R.H. Mathiesen, Y. Houltz, J. Li, C. Lockowandt, K. Henriksson, G. Zimmermann, N. Melville, D.J. Browne, XRMON-SOL: Isothermal equiaxed solidification of a grain refined Al–20 wt%Cu alloy, J. Cryst. Growth 440 (2016) 38-46.
[60] H. Nguyen-Thi, G. Reinhart, G. Salloum Abou Jaoude, R.H. Mathiesen, G. Zimmermann, Y. Houltz, D. Voss, A. Verga, D.J. Browne, A.G. Murphy, XRMON-GF: A novel facility for solidification of metallic alloys with in situ and time-resolved X-ray radiographic characterization in microgravity conditions, J. Cryst. Growth 374(0) (2013) 23-30.
[61] A.G. Murphy, D.J. Browne, W.U. Mirihanage, R.H. Mathiesen, Combined in situ X-ray radiographic observations and post-solidification metallographic characterisation of eutectic transformations in Al–Cu alloy systems, Acta Mater. 61(12) (2013) 4559-4571.
[62] https://imagej.nih.gov/ij/index.html. https://imagej.nih.gov/ij/index.html).
[63] W.W. Mullins, R.F. Sekerka, Morphological Stability of a Particle Growing by Diffusion or Heat Flow, J. Appl. Phys. 34(2) (1963) 323-329.
[64] Ø. Nielsen, A. Mo, B. Appolaire, H. Combeau, Measurements and modeling of the microstructural morphology during equiaxed solidification of Al-Cu alloys, Metall. Mater. Trans. A 32(8) (2001) 2049-2060.
[65] M. Wu, A. Ludwig, Modeling equiaxed solidification with melt convection and grain sedimentation—I: Model description, Acta Mater. 57(19) (2009) 5621-5631.
[66] M. Rappaz, P.H. Thévoz, Solute diffusion model for equiaxed dendritic growth, Acta Metall. 35(7) (1987) 1487-1497.

[67] C.Y. Wang, C. Beckermann, A multiphase solute diffusion model for dendritic alloy solidification, Metall. Trans. A 24(12) (1993) 2787-2802.
[68] L. Nastac, D.M. Stefanescu, Macrotransport-solidification kinetics modeling of equiaxed dendritic growth: Part I. Model development and discussion, Metall. Mater. Trans. A 27(12) (1996) 4061-4074.
[69] W. Kurz, D.J. Fisher, Dendrite growth at the limit of stability: tip radius and spacing, Acta Metall. 29(1) (1981) 11-20.
[70] W. Kurz, D.J. Fisher, Fundamentals of Solidification, 4th ed., Trans Tech Publication LTD1998.
[71] H. Men, B. Jiang, Z. Fan, Mechanisms of grain refinement by intensive shearing of AZ91 alloy melt, Acta Mater. 58(19) (2010) 6526-6534.
[72] W. Heyroth, R. Gerloff, Scanning electron microscopic determination of the particle size distribution of an agglomerating phase in a metallic melt, Z. Metallk. 87(9) (1996) 684-690.
[73] A. Tronche, Investigation and Modelling of Inoculation of Aluminium by TiC, University of Cambridge, 2001.
[74] M. Wu, A. Ludwig, Modeling equiaxed solidification with melt convection and grain sedimentation—II. Model verification, Acta Mater. 57(19) (2009) 5632-5644.
[75] R. Gerloff, W. Heyroth, W. Reif, U. Schmidt, T. Wand, The agglomeration of the TiB2-phase which has been added to molten aluminium for the grain refinement, Metall 50(2) (1996) 97-101.
[76] T.E.Quested, Solidification of Inoculated Aluminium Alloys, University of Cambridge, Cambridge UK, 2004.
[77] M. Rappaz, P.H. Thévoz, Solute diffusion model for equiaxed dendritic growth: Analytical solution, Acta Metall. 35(12) (1987) 2929-2933.
[78] M. Rappaz, W.J. Boettinger, On dendritic solidification of multicomponent alloys with unequal liquid diffusion coefficients, Acta Mater. 47(11) (1999) 3205-3219.

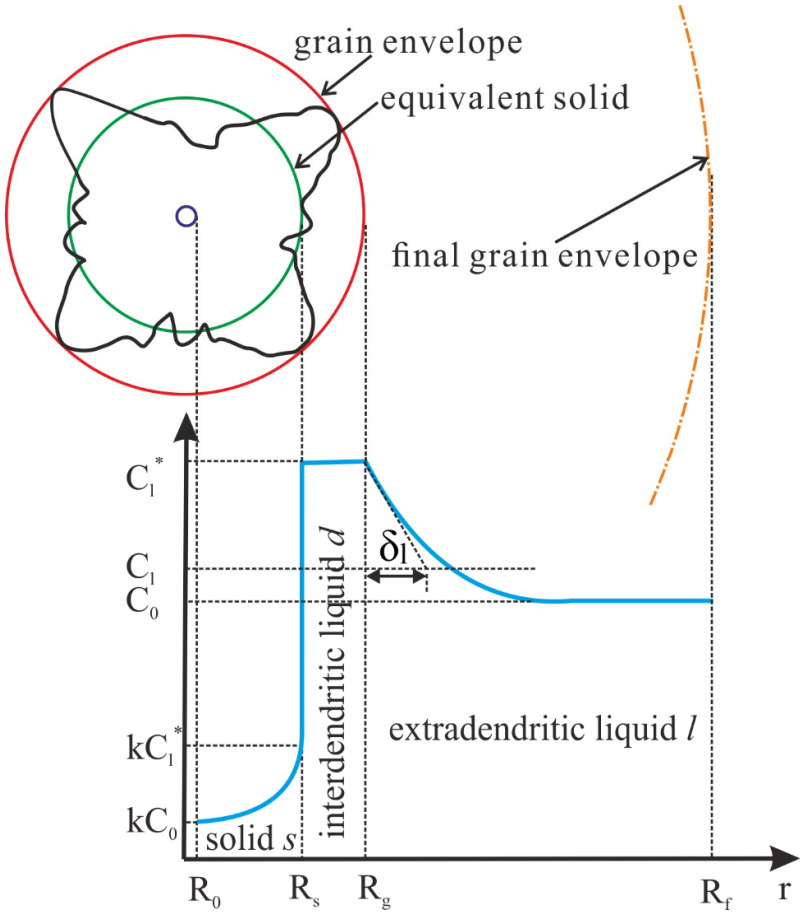

Fig. 1. A schematic representation of the solute diffusion model for equiaxed dendritic growth, in which three regions or phases are discriminated: solid *s*, interdendritic liquid *d* and extradendritic liquid *l* and the corresponding concentration profile in each phase.

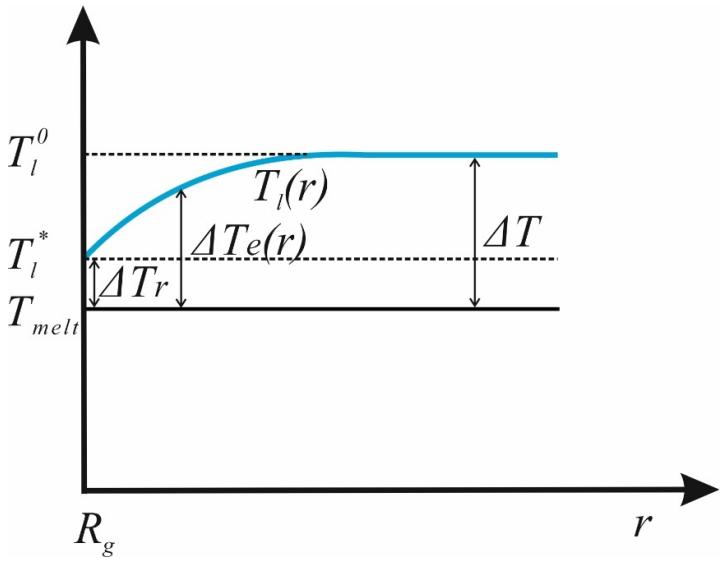

Fig. 2. Liquidus temperature $T_l(r)$and the corresponding local undercooling $\Delta T_e(r)$ of the liquid surrounding the growing grain. In the figure, T_{melt} is the real temperature of melt, T_l^* the liquidus temperature at the s/l interface and T_l^0 the liquidus temperature of the bulk liquid outside of solute diffusion layer; ΔT_r and ΔT are curvature undercooling and maximum undercooling in the bulk melt, respectively.

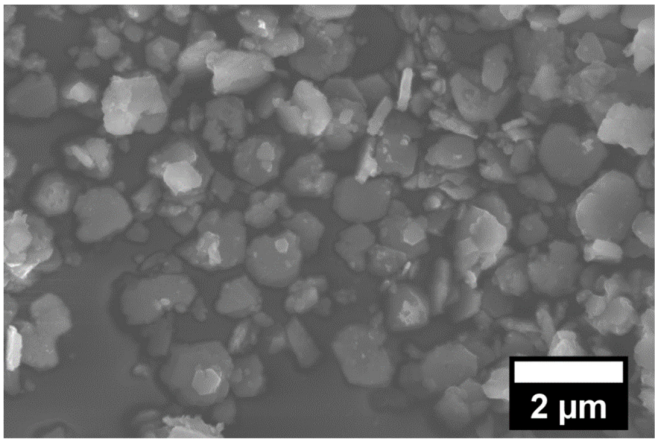

Fig. 3. SEM micrograph of TiB_2 particles collected from the dissolved Al-5Ti-1B master alloy.

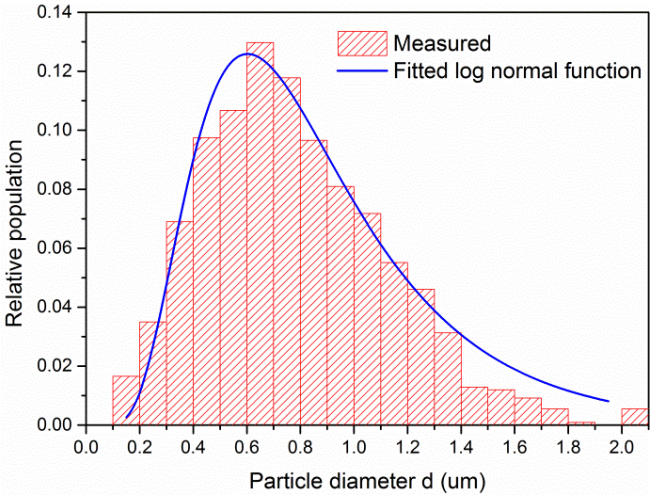

Fig. 4. Measured size distribution of the TiB_2 particles in the Al-5Ti-1B master alloy and the fitted log-normal distribution.

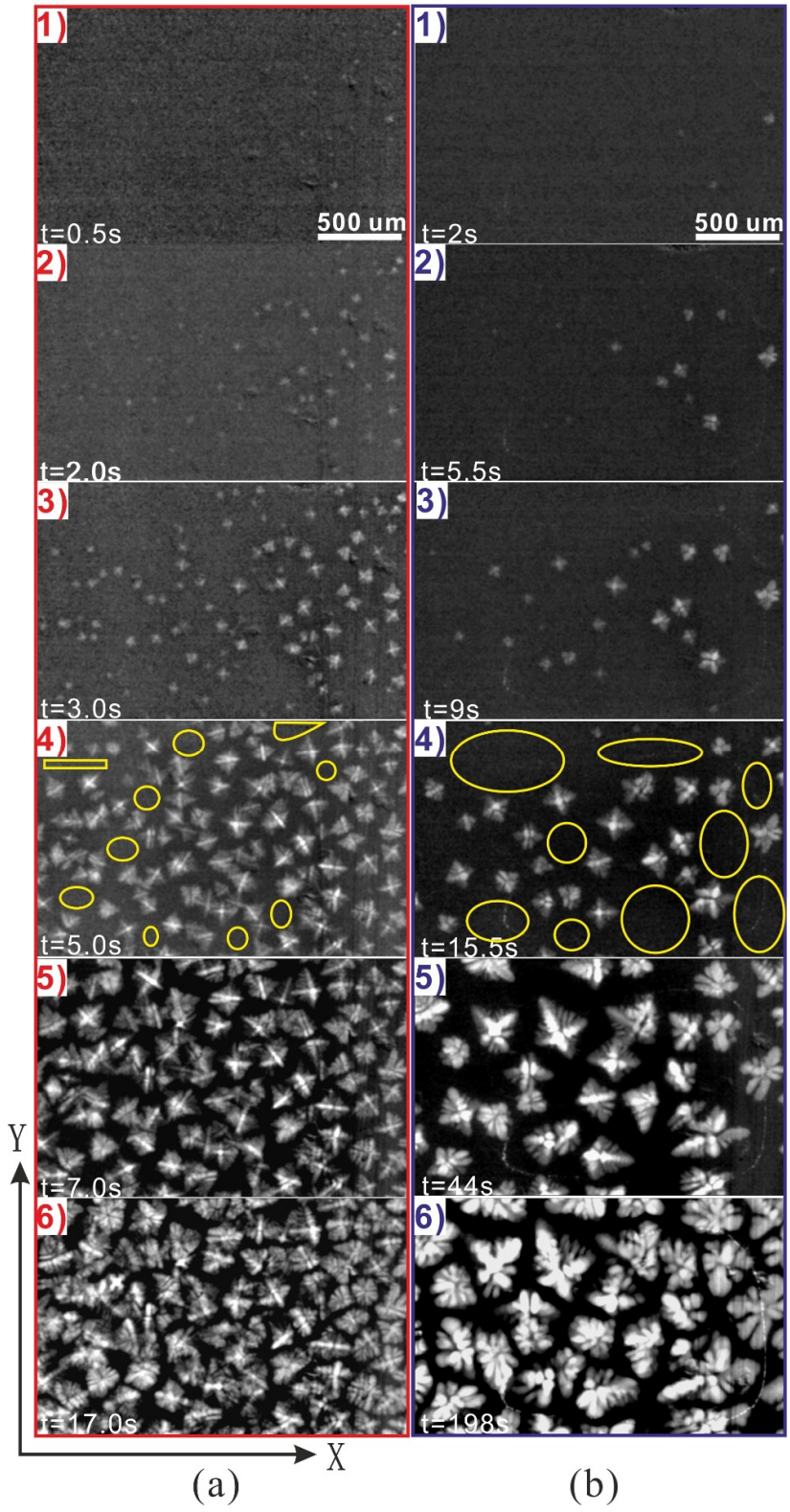

Fig. 5. Selected frames from the in-situ X-radiography studies of solidification in Al-10wt.%Cu alloy inoculated with 0.05 wt.% Al-5Ti-1B grain refiner, under continuous cooling-down at two different cooling rates, (a) 0.5 K/s and (b) 0.05 K/s.

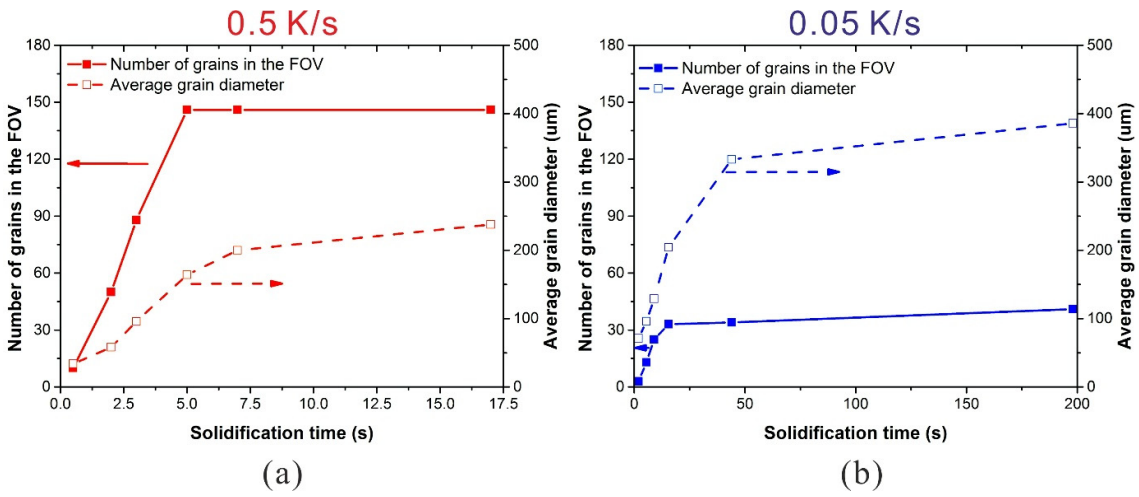

Fig. 6. The evolution of total number of grains and average circular equivalent diameter of grain as a function of solidification time since the first grain appears in the FOV (extracted from X-radiography images shown in Fig. 5).

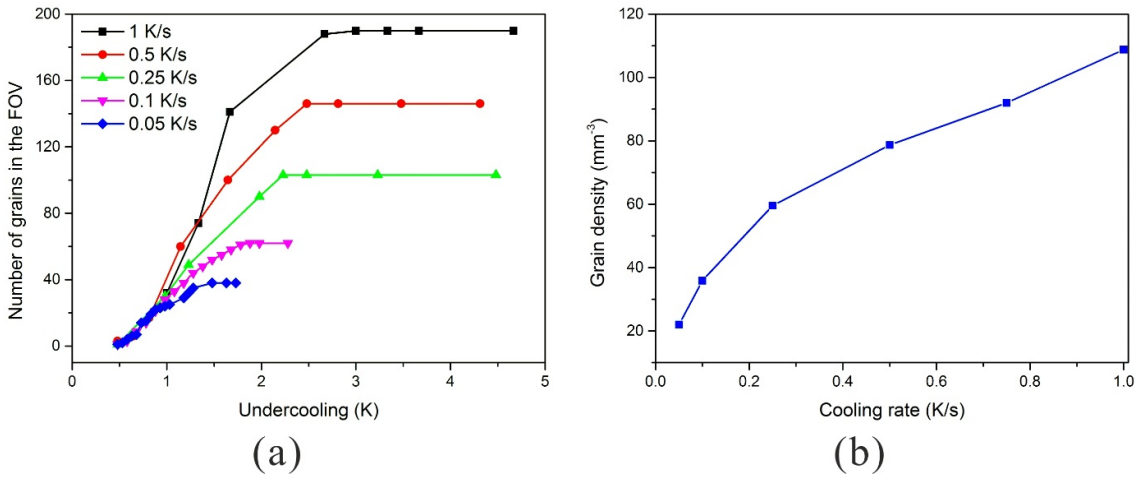

Fig. 7. (a) The evolution of total number of grains in the FOV as a function of undercooling for the 0.05 wt.% grain refiner inoculated Al-10wt.%Cu alloy solidified at different cooling rates (including 0.5 K/s and 0.05 K/s cases shown in Fig. 6). (b) Final grain density as a function of cooling rate for the same alloy.

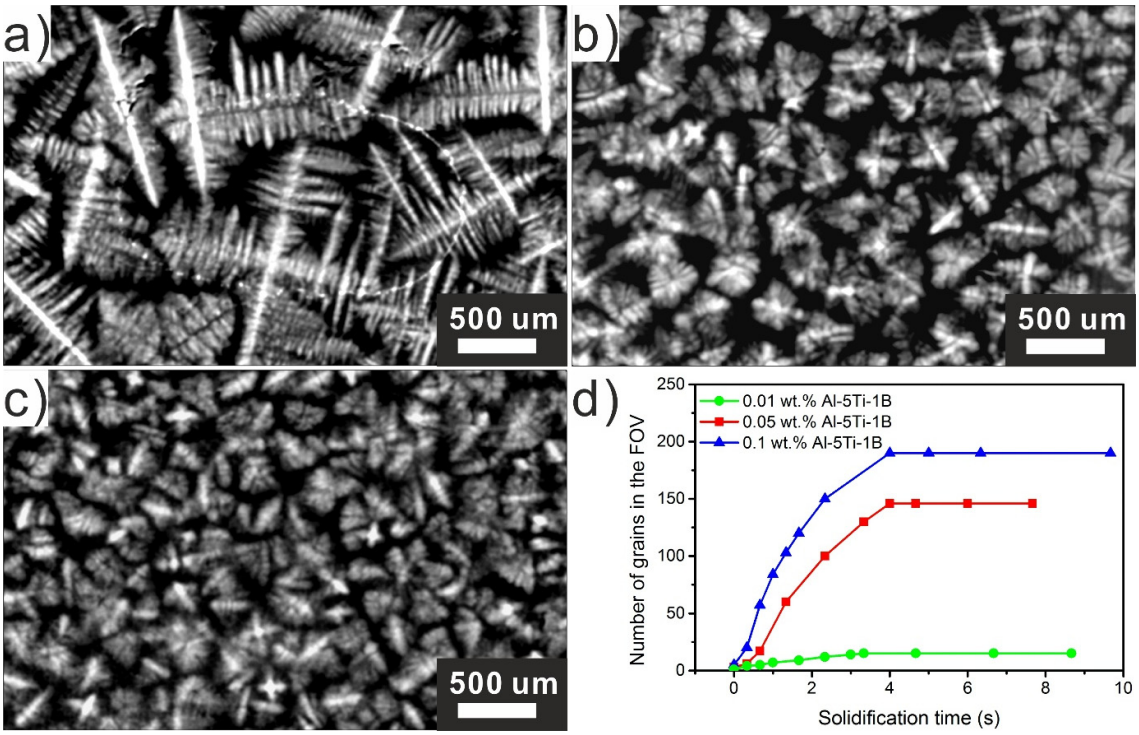

Fig. 8. Selected X-radiography images collected during solidification of Al-10wt.%Cu alloy with different addition level of Al-5Ti-1B, (a) 0.01, (b) 0.05 and (c) 0.1 wt.% under 0.5 K/s cooling rate and (d) the corresponding evolution of total number of grains in the FOV as a function of solidification time.

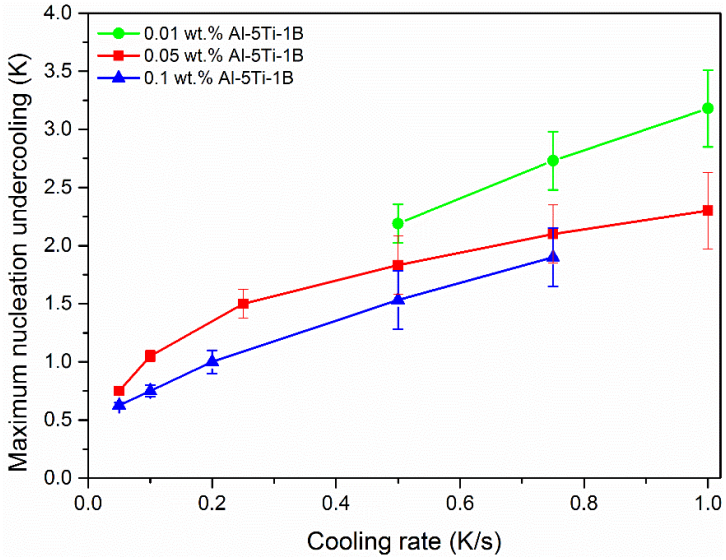

Fig. 9. Maximum nucleation undercooling of Al-10wt.%Cu alloy inoculated with 0.01, 0.05 and 0.1 wt.% Al-5Ti-1B as a function of cooling rate as measured from in-situ X-radiographic image sequences.

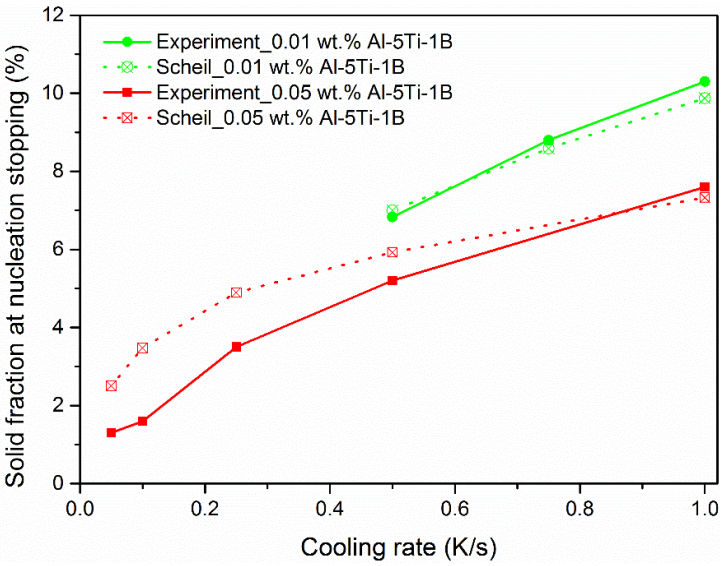

Fig. 10. Measured solid volume fractions of grains at nucleation ceasing for the Al-10wt.%Cu alloy inoculated with 0.01 and 0.05 wt.% Al-5Ti-1B as a function of cooling rate and the corresponding predictions by Scheil equation.

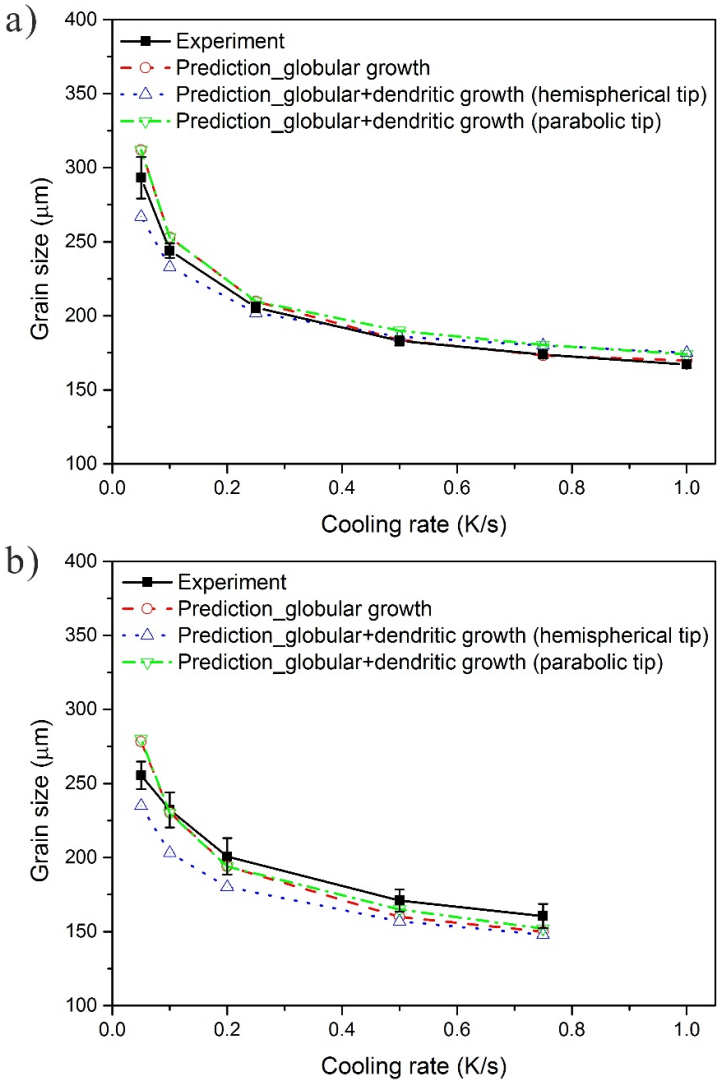

Fig. 11. Measured and predicted grain sizes based on three different growth kinetics as a function of cooling rate for (a) 0.05 wt.% and (b) 0.1 wt.% Al-5Ti-1B inoculated Al-10wt.%Cu alloy.

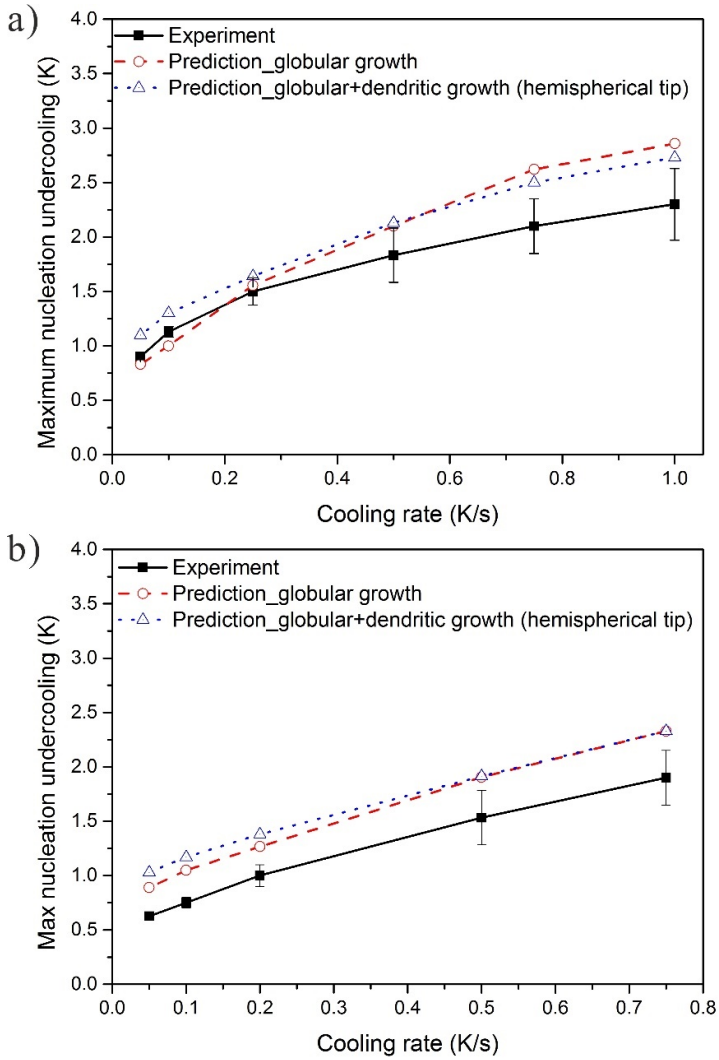

Fig. 12. Predicted and experimentally determined maximum nucleation undercooling of Al-10wt.%Cu alloy inoculated with (a) 0.05 wt.% and (b) 0.1 wt.% Al-5Ti-1B solidified under different cooling rates. Two different growth kinetics were compared.

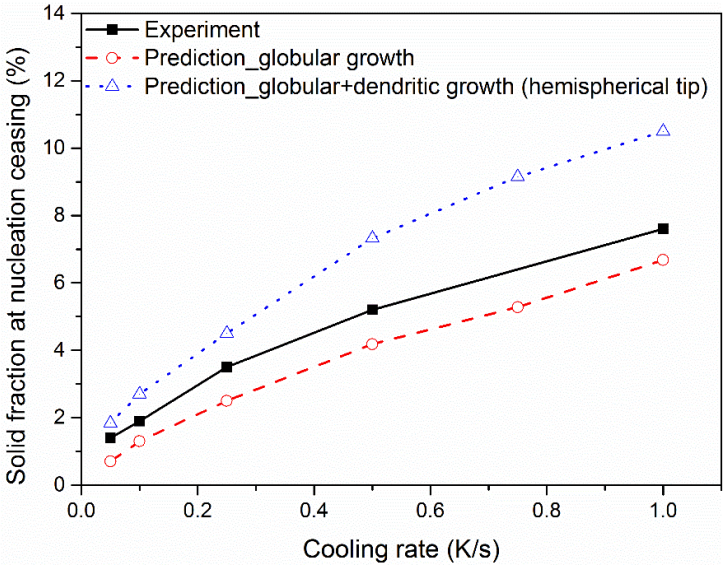

Fig. 13. Predicted and experimentally determined solid volume fraction at nucleation ceasing of Al-10wt.%Cu alloy inoculated with 0.05 wt.% Al-5Ti-1B solidified under different cooling rates. Two different grain growth kinetics were compared.

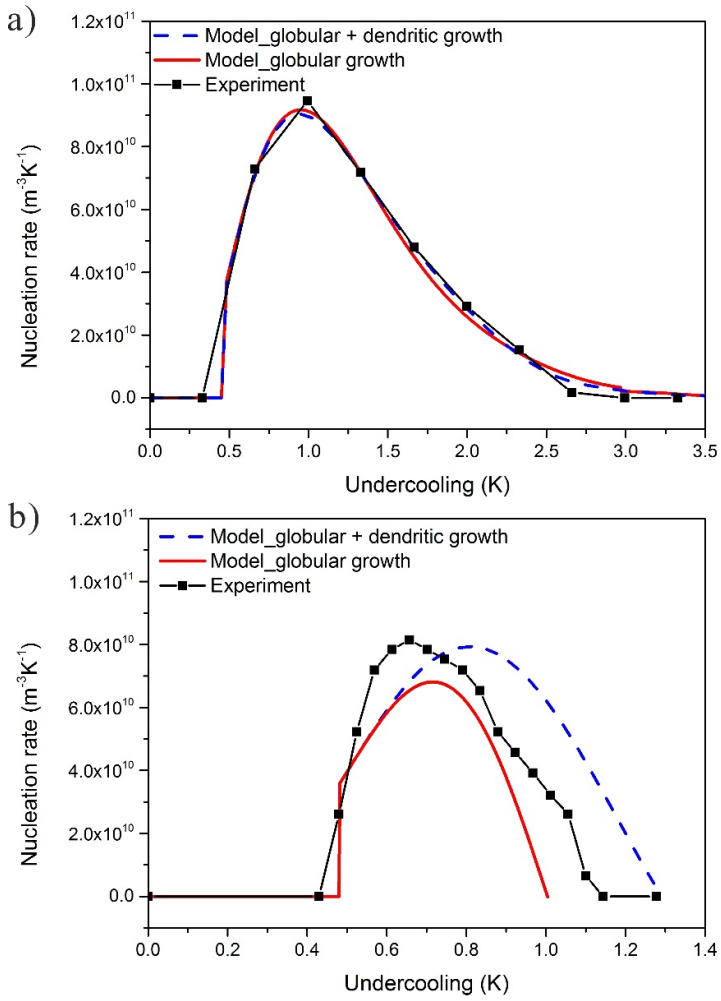

Fig. 14. Predicted and experimentally measured nucleation rates of Al-10wt.%Cu alloy inoculated with 0.05 wt.% Al-5Ti-1B grain refiner as a function of undercooling during solidification under (a) 1 K/s and (b) 0.1 K/s cooling rate. Two grain growth kinetics were compared.

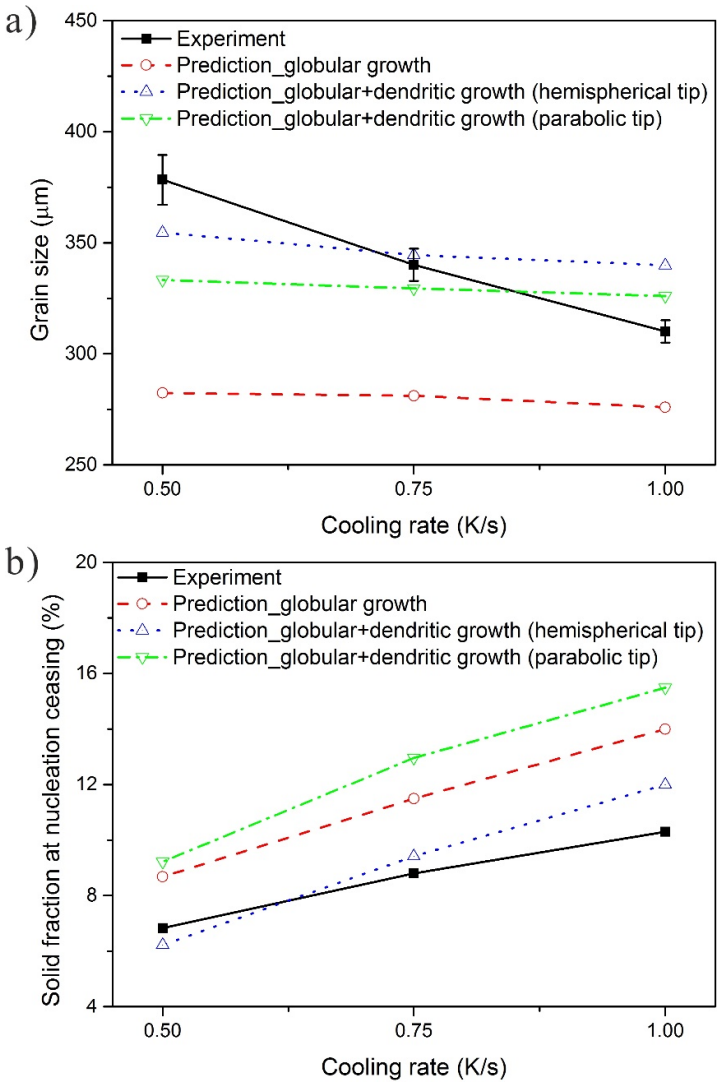

Fig. 15. (a) Measured and predicted grain size, and (b) solid volume fraction at nucleation ceasing as a function of cooling rate for 0.01 wt.% Al-5Ti-1B inoculated Al-10wt.%Cu alloy.

Table 1. Physical parameters used in the model calculations.

Quantity	Symbol	Units	Value	Ref.
Gibbs-Thomson coefficient	Γ	m K	2.41×10^{-7}	[33]
Diffusion coefficient in Al melt (Cu)	D_l	$m^2\ s^{-1}$	4.65×10^{-9}	[25]
Liquidus slope	m	K wt.%$^{-1}$	-3.4	[25]
Partition coefficient	k		0.14	[25]